The invasive lobular cancer cell line encyclopedia (ICLE) for studying potential biomarkers and exploring therapeutic opportunities

Osama Shiraz Shah[1,5], Fangyuan Chen[2,5], Abdalla Webn[3,5], Anokhi Kashiparekh[4], Laura Savariau[4,5], Benjamin Clifford[6], Jagmohan Hooda[5], Jennifer M Atkinson[5], Steffi Oesterreich[3,5,7], Adrian V. Lee[3,5,7,8]

[1]Integrative Systems Biology, School of Medicine, University of Pittsburgh
[2]School of Medicine, Tsinghua University, Beijing, China
[3]Department of Pharmacology & Chemical Biology, University of Pittsburgh
[4]Department of Human Genetics, School of Public Health, University of Pittsburgh
[5]Womens Cancer Research Center at UPMC Hillman Cancer Center and Magee Women's Research Institute, Pittsburgh, PA
[6]Bionano, San Diego, California, USA
[7]Department of Pharmacology & Chemical Biology, University of Pittsburgh, Pittsburgh, PA
[8]Institute for Precision Medicine, University of Pittsburgh and UPMC, Pittsburgh, PA

*Steffi Oesterreich and Adrian Lee share senior authorship

Corresponding Author: Steffi Oesterreich, University of Pittsburgh, 5051 Centre Ave, Pittsburgh, PA 15213. Phone: 412-641-8555, Fax: 412-641-7724, E-mail: oesterreichs@upmc.edu. Adrian V. Lee, University of Pittsburgh, 5051 Centre Ave, Pittsburgh, PA 15213. E-mail: leeav@upmc.edu.

Abstract

Invasive lobular carcinoma (ILC), the most common histological "special type" of breast cancer, accounts for ~10-15% of all breast cancer diagnoses and is characterized by unique clinical features and metastatic spread. Despite the unique pathobiology of ILC, studies of how its molecular alterations can be linked to new treatments have been hindered by the scarcity of well-characterized cell line models. To address this, we generated the ILC Cell Line Encyclopedia (ICLE), a comprehensive multi-omic characterization of cell lines derived from ILC or cell lines referred to as ILC-like derived from unannotated tumors with features of ILC such as loss of E-cadherin. Using consensus multi-omic subtyping, we confirmed the luminal status of previously established ILC cell lines and uncovered additional ILC/ILC-like cell lines with luminal features and RNA/DNA copy number similarity to ILC tumors. ICLE cell lines retained molecular alterations in key ILC genes at a similar frequency to both primary and metastatic ILC tumors. Importantly, ICLE cell lines recapitulated the *CDH1* alteration landscape of ILC tumors including enrichment of truncating mutations and biallelic inactivation of *CDH1*. Optical genome mapping uncovered novel genomic rearrangements including structural variations in *CDH1* and other functional gene fusions and revealed breast cancer specific patterns of chromothripsis in chromosomes 8, 11 and 17. Aberrant DNAm events and integrative analysis with RNA expression revealed epigenetic activation of *TFAP2B*, an emerging biomarker preferentially expressed in lobular disease. Finally, towards the goal of identifying novel druggable vulnerabilities in ILC, publicly available RNAi loss of function breast cancer cell line datasets revealed numerous putative vulnerabilities cytoskeletal components, focal adhesion and

PI3K/AKT pathway in ICLE vs NST cell lines. We addressed the lack of suitable models to study E-cadherin deficient breast cancers by comprehensively characterizing multi-omic features of both established and putative ILC models and showed their similarity to tumors and highlighting novel druggable vulnerabilities.

Introduction

Invasive lobular carcinoma (ILC), the most common histological "special type" of breast cancer (BC), accounts for approximately 10-15% of all BC diagnoses. It is characterized by unique features such as E-cadherin loss/deficiency, lower grade, hormone receptor positivity, larger diffuse tumors, distinctive metastatic patterns and unique molecular alterations (1–7). Despite ILC being acknowledged as a disease with distinct biology that necessitates specialized and precision medicine treatments, the identification of new treatments has been hindered by the scarcity of well-characterized cell line models (8–10).

Pioneering large-scale cancer cell line characterization studies, including those by Ghandi et al (11), Marcotte et al (12), Iorio et al (13), and others (14,15), have revealed multi-omic molecular attributes and gene dependencies of diverse cancer cell lines. These investigations have facilitated a systematic selection of preclinical models that mirror the molecular characteristics of human cancers, enabling a more precise modeling of specific subtypes of breast cancer (such as the claudin-low and HER2-enriched types) and the exploration of their unique molecular alterations within the context of tumor initiation, progression, metastasis, resistance to treatments, and the development of new therapies (12–14,16). Comprehensive multi-omic characterization of cancer cell lines has been invaluable in advancing precision medicine research (14,16–23). However, a mere eight ILC cell lines have been established and made publicly available, of which only four (namely MDAMB134VI, MDAMB330, SUM44PE and BCK4) are established ER+ cell lines and are frequently utilized for modeling human-ILC disease (8,9,24–27). The remaining ILC cell lines have been inadequately

characterized with only a few literature reports mentioning their use (8,9). Several factors can explain this limited availability and poor characterization including the lower incidence of ILC, the fewer number of ILC cases enrolled in clinical trials, the recent understanding of ILC as a unique disease, the fact that certain ILC cell lines are not yet publicly available/purchasable (including MA11 and WCRC25), and the intrinsic characteristics of ILC that make it challenging to culture them as cell lines (2,8,9,28).

The RATHER consortium previously noted that a number of breast cancer cell lines annotated as “carcinoma”, “adenocarcinoma” or “ductal carcinoma” harbor genomic loss of *CDH1* or its binding partner *CTNNA1* (29). These cell lines were labeled as “ILC-like” cell lines and proposed as potential models to study ILC. However, since many of these ILC-like cell lines were established before ILC was recognized as a unique disease, it remains unclear whether these cell lines originated from ILC tumors or could serve as faithful models of this disease.

To address this, we generated the ILC Cell Line Encyclopedia (ICLE), a comprehensive multi-omic characterization of ILC and ILC-like cell lines. ICLE cell lines exhibited pathognomonic E-cadherin deficiency and retained key ILC molecular alterations seen in tumors. Through optical genome mapping, we characterized chromothripsis events and discovered novel genomic rearrangements, including new structural deletions in *CDH1* and other functional gene fusions. Additionally, we systematically analyzed aberrant DNAm events and integrative analysis with RNA expression revealed the epigenetic regulation of *TFAP2B*, a putative lobular biomarker. Analysis of RNAi/CRISPR screens revealed druggable targets in PI3K/mTOR and focal adhesion pathways. Finally, we propose a qualitative and quantitative scheme to aid in rational selection of ICLE cell lines for modeling human ILC disease. In summary, we generated ICLE the

first ILC cell line encyclopedia, highlighting key molecular features, cataloging druggable targets and presenting a scheme for rational model selection.

Materials and Methods

Multi-omic Profiling of ILC and ILC-like Cell Lines

ILC/ILC-like Cell Line Collection, Culturing and Extraction of RNA, DNA and protein lysates: All known *CDH1*/E-cadherin or *CTNNA1*/α-catenin deficient ILC/ILC-like cell lines have been reported in the literature (ILC-like cell lines were reported in Michaut et al study (29)) (Supplementary Table S1). Two ILC-like cell lines (SKBR5 and ESVA-T) were not purchasable at the time of collection and were excluded from the study. WCRC25, an ILC cell line established and reported in our previous study (30) was also included in this study. The final panel comprising of 17 ILC/ILC-like cell lines, that were either purchased from a vendor or acquired through material transfer agreement (MTA), included BCK4 (Asterand), CAMA1 (ATCC), MDAMB134VI (ATCC), HCC2185 (ATCC), IPH926 (DSMZ), MDAMB330 (ATCC), SUM44PE (Asterand), UACC3133 (ATCC), WCRC25 (inhouse), 600MPE (Asterand), HCC1187 (ATCC), HCC2218 (ATCC), MDAMB453 (ATCC), MDAMB468 (ATCC), SKBR3 (ATCC), OCUBM (MTA - Riken) and Z7530 (ATCC). All cell lines were cultured using the vendor recommended media conditions and underwent STR profiling based authenticated at the Arizona genetics core. All cell lines were routinely (after every few passages and before extraction of RNA, DNA and protein lysates) assayed to avoid Mycoplasma contamination using Lonza MycoAltert mycoplasma detection kit (Cat # LT07-118) and/or ABM mycoplasma PCR detection kit (Cat # G238) as per manufacturer's instructions. Cell lines were grown in 150mm plates and used for RNA, DNA, and protein lysate collection when at ~70% confluency. DNA extraction was performed using

116 Qiagen QIAamp DNA mini kit (Cat # 56304) and RNA extraction using Qiagen RNeasy kit (Cat #
117 74004) as per vendor recommendations. All DNA/RNA samples showed high quality (260/280
118 ratio ~1.8 for DNA and ~2.0 for RNA) using NanoDrop (Cat # ND-2000). Protein lysates were
119 prepared in accordance with the MD-Anderson RPPA core facility
120 (https://www.mdanderson.org/research/research-resources/core-facilities/functional-
121 proteomics-rppa-core/antibody-information-and-protocols.html) (31).
122 RNA sequencing (RNAseq) and data analysis: Extracted total RNA for all cell lines was sent
123 to the UPMC Genome Center for RNAseq library preparation and sequencing. Briefly, RNA
124 concentrations were quantified by ThermoFisher Qubit (Cat # Q33238) and their size
125 distribution measured by Agilent TapeStation (Cat # G2991AA). Paired-end RNAseq libraries
126 were prepared using KAPA poly A RNA hyperPrep kit (Cat # 8098093702), and sequenced with
127 NovaSeq 6000 for a target of 100 million reads/sample using S1 reagents for 300 cycles, 0.8
128 billion reads and total output of 250G (Cat # 20028317). Quality control of fastq files was
129 performed using FastQC v0.11.9 (32) and summarized with multiQC (33). fastq files were
130 aligned to hg38 reference transcriptome using STAR v2.7.5a (34) and gene count files generated
131 using subread v2.0.1 featureCounts function (35). Gene counts were converted to counts per
132 million (CPM) and log2 normalized using EdgeR (36) for downstream analyses in R (37). Ghandi
133 et al 2019 (CCLE study) (11) RNAseq files were reprocessed using the pipeline described above
134 and then gene counts merged with ICLE dataset to generate an integrated breast cancer cell
135 line gene count matrix. Sensitivity to endocrine therapy was predicted using difference
136 between ERpos and ERneg gene signatures as described previously (38).

137 Whole-exome sequencing (WES) and data analysis: Extracted DNA for all cancer cell lines
138 (plus two control blood lines HCC1187BL and HCC2218BL) was sent to the UPMC Genome
139 Center for WES library preparation and sequencing. Paired end libraries were prepared using
140 Roche KAPA Hyper Plus Kit (Cat # 09075810001). Briefly, 500 ng of DNA was processed by
141 fragmentation, enzymatic end repair, A-tailing and ligation. Quality control was done using
142 Agilent Fragment analyzer. Exonic regions were captured using IDT xGen Exome Research Panel
143 v1.0 (Cat # 1056114) with xGen Universal Blockers (Cat # 1075474) and Roche KAPA HyperCap
144 workflow 3.0 (Roche) according to manufacturer protocol. The library size assessment was
145 done using Fragment Analyzer (Agilent). Libraries with an average size of 400 bp (range: 200-
146 600bp) were quantified by qPCR on the LightCycler 480 (Roche) using the KAPA qPCR
147 quantification kit (Roche). The libraries were normalized and pooled as per manufacturer
148 protocol (Illumina). Sequencing was performed using NovaSeq 6000 platform (Illumina) with
149 151 paired-end reads to an average target depth of 30-50X for germline and 125X coverage for
150 somatic samples using S1 reagents for 300 cycles, 0.8 billion reads and total output of 250G (Cat
151 # 20028317). Quality control of fastq files was performed using FastQC tool (32) and aligned to
152 hg38 using BWA MEM tool (39). Variant calling was performed as per GATK best practices
153 (Somatic short variant discovery (SNVs + Indels) – GATK (broadinstitute.org)). Briefly, GATK v4
154 MuTect2 pipeline (40) was used for calling single nucleotide variations (SNV) and indels with
155 default parameters using HCC1187BL and HCC2218BL blood lines as normal control. All
156 mutations were annotated using Ensemble variant effect predictor (VEP) (41) and converted to
157 MAF format. Common polymorphisms (present in 1000genome database (42)), silent mutations
158 and mutations with allele frequency < 10% were removed before further analyses. Ghandi et al

2019 (CCLE study) MAF files filtered in similar way and merged with ICLE dataset to generate an integrated breast cancer cell line MAF file for downstream use. Tumor mutation burden (TMB) was computed using R package Maftools (43). Exonic deletions in *CDH1* and *CTNNA1* gene canonical isoforms were identified using samtools bedcov function.

Bionano optical genome mapping (OGM): Frozen cell pellets containing at least 1.5 million cells were sent to Bionano Genomics Core, CA for OGM. Briefly, high molecular weight DNA (≥ 150 kbp) was extracted using Bionano SP Blood and Cell Culture DNA Isolation Kit (Cat # 80042). DNA concentrations were measured using Qubit Broad Range assay (Cat # Q32850) and labelled using Bionano Direct Label and Stain (DLS) labelling kit (Cat # 80005). Labelled DNA was transferred to a flow cell of a Saphyr G2.3. chip (Cat # 20366) and scanned repeatedly using a Saphyr System with Bionano Access Server (Cat # 90067). The resulting images of molecules were converted to digital molecules. These molecules were aligned to reference genome maps to result in consensus whole-genome maps. Bionano solve v3.5 rare variant analysis and copy number analysis pipelines were used to detect structural variations, copy number variations and fusions at a minimum lower resolution of 5KB. The resulting structural variations were filtered against a panel of controls to remove pipeline artifacts and germline variations using Bionano Access Software v1.7. Filtered data was downloaded and further analyzed in R. All structural variations were categorized as one of the following: deletions (Del), insertions (Ins), inversions (Inv), duplications (Dup), inter-chromosomal translocations (Transloc-inter), and intra-chromosomal translocations (Transloc-intra). Correlation between structural variation count, mutation count and chromosome size were performed using Pearson correlation.

180 Chromothripsis events were characterized using shatterseek tool using default parameters (44).
181 Circos plots were generated using interacCricos (45).
182 Reverse Phase Protein Array (RPPA): Protein lysates were sonicated and centrifuged at
183 14000rpm. Protein concentrations were determined by BCA. Then lysates were mixed with 4X
184 SDS to have final concentration of 1ug/ml and then sent to RPPA core facility at MD Anderson
185 Cancer Center, TX for RPPA. Briefly, the lysate was diluted and arrayed on nitrocellulose-coated
186 slides and probed with antibodies to recognize signaling molecules. Signals are captured by DAB
187 colorimetric reaction followed by spots are detection, background correction (using internal
188 controls) and spot quality control. Curve fitting is used to quantify net relative concentrations
189 and data is normalized for loading differences and other sources of variations. Final data
190 comprised of ~450 proteins and phospho-proteins. Marcotte et al 2016 (Neel Lab) (12)
191 normalized RPPA dataset was merged with normalized ICLE RPPA dataset to generate an
192 integrated breast cancer cell RPPA dataset for downstream use.
193 Illumina DNA Methylation (DNAm) Array: Extracted DNA for all cell lines (except SKRB-3)
194 was sent to University of Pittsburgh Genomic Research Core for DNA methylation profiling
195 using Illumina Infinium Methylation EPIC BeadChip Kit (Cat # WG-317-1001). Briefly, DNA was
196 quantified by Qubit and 500ng of DNA per sample was bisulfite converted using Zymo EZ DNA
197 methylation kit (Cat # D5003) following vender recommendations. Bisulfite-converted DNA was
198 hybridized to BeadChips and analyzed on an Illumina iScan as per vender recommendations.
199 Resulting raw IDAT files underwent quality control and preprocessing to result in B-values for
200 850K methylation probes using R package SeSAMe (46). B values were defined as SM/(SM + SU)
201 for each methylation probe, where SM and SU represent signal intensities for methylated and

unmethylated alleles. Probes with P value > 0.05 were masked as NA before downstream analysis. Probes were annotated for genomic context using Infinium annotations (47). Iorio et al 2016 (Sanger) (13) Infinium Methylation 450K array dataset was reprocessed using the pipeline described above and merged with ICLE EPIC array dataset to generate an integrated breast cancer DNAm dataset for downstream use.

Illumina CytoSNP Array: Extracted DNA for all cell lines (except SKRB-3) was sent to University of Pittsburgh Genomic Research Core for SNP profiling using Illumina Infinium CytoSNP-850K v1.2 BeadChip Kit (Cat # 20025644). Briefly, DNA was quantified using Qubit and 750 ng of DNA was amplified, fragmented, precipitated and hybridized to BeadChips and then analyzed on an Illumina iScan as per vendor protocol. Resulting raw IDAT files underwent quality control and preprocessing using Illumina Genome Studio version 2.0. Copy number (CN) analysis was performed using its CNVpartition v3.2.0 plugin. Copy number logR-ratio, B-allele frequencies (BAF) and genotype calls were exported and further analyzed in R. Copy number data was segmented using R package DNAcopy (48) and significantly amplified and deleted regions across samples were identified using GISTIC analysis (49). Marcotte et al 2016 (Neel Lab) (12) Illumina Omni Quad CN and SNP dataset was reprocessed using above pipeline and merged with ICLE CN and SNP dataset to generate integrated breast cancer cell line CN and SNP dataset. Fraction of genome altered (FGA) was computed using R package CINmeterics (50) by using segmented copy number.

The generated ICLE dataset data types are summarized in Supplementary Table S2, and the public datasets used for integration are summarized in Supplementary Table S3. The overlapping cell lines between ICLE and other public datasets showed strong genotyping

similarity (Supplementary Figure S1). Mutations and copy number alterations were combined to define a single molecular/genomic alterations matrix for use in downstream analyses. All alterations were summarized into the following categories: mutation (MUT), mutation + LOH (MUT;LOH), mutation + single copy gain (MUT;GAIN), amplification (AMP) and deletions (DEL).

Molecular Subtypes

PAM50 subtyping was performed using R package genefu (51). This tool uses the method established in the Parker et al study (52). Briefly, Parker et al identified 50 genes that define transcriptional subtypes of breast cancer. Based on this training cohort of N=139, genefu computes PAM50 scores for a given input data. The PAM50 scores represent the correlation strength of each input sample to each PAM50 centroid in the training dataset. Final PAM50 subtype is defined as the one to which a given input sample has the strongest correlation score.

Consensus Clustering was performed individually on each integrated dataset to identify mRNA, RPPA and DNAm subtypes using ConsensusClusterPlus R (53). Briefly, ConsensusClusterPlus function was run on top 10% variable features with 1000 repeats and K = 9. Resulting clusters were evaluated based on their molecular features including E-cadherin, ER-A, PR, HER2, Cluadin-7 protein levels and ERpos/ERneg gene signature (adapted from Symmans et al (38)) scores. ERpos/ERneg signature scores were defined as mean expression of CPM values of each gene in the signature. Clusters with similar molecular features were combined into a single cluster. Final subtypes were defined as following; Luminal (Lum) subtype comprised of cell lines with high ER-A/PR and low HER2/phospho-HER2 expression and had high

ERpos gene signature score, HER2 subtype comprised of cell lines with low ER-A/PR and very high HER2/phospho-HER2 protein expression (due to HER2/ERBB2 gene amplifications) and had low ERpos gene signature score, Luminal/HER2 (Lum/HER2) subtype comprised of cell lines with high HER2/phospho-HER2 expression (due to HER2/ERBB2 gene amplifications) but unlike HER2 subtype showed similarity to Lum cluster and also had medium to high ERpos gene signature score, Basal subtype comprised of low ER-A/PR/HER2 cell lines and finally Claudin low (ClaudinLow) subtype comprised of basal cell lines which also had low levels of Claudin-7, a subset of ClaudinLow subtype cells showed down-regulation of E-cadherin and epithelial to mesenchymal (EMT) phenotype and were referred to as ClaudinLow/EMT. The results are shown in Supplementary Figure S2-S4 A-D and Figure 1B.

Molecular Resemblance to Tumors & *CDH1* Alteration Landscape

The molecular resemblance of ILC/ILC-like cell lines to ILC tumors was assessed by comparing copy number profiles and molecular alteration frequency in key ILC genes. TCGA Primary ILC tumor (3) and MSK Metastatic ILC tumor (54) genome-wide segmented copy number, gene-level GISTIC values and mutation MAF datasets were acquired from cbioportal (55). Genome-wide segmented copy number profiles were visualized using integrative genomics viewer (IGV) (56) and key copy number events were visually compared between tumors and with cell lines. For a more quantitative comparison, we quantified similarity of tumor and cell line copy number profiles by Pearson correlation. Since there is a strong association between copy number values for genomically proximal loci the required data

independence assumptions are invalidated. Instead, we used a sampling approach by randomly selecting 5 genes per genomic cytoband. Copy number values for these randomly selected genes in all cell lines were correlated with mean copy number profiles of TCGA ILC tumors (Figure 6B). Similarly, we quantified similarity of tumors and cell lines RNA expression using Pearson correlation. Since tumors also comprise of stroma, only the top 100 highly and lowly expressed genes in ILC tumors were used for correlation between all cell lines with mean expression of TCGA ILC tumors (Figure 6B).

Molecular/genomic alteration matrix for primary and metastatic ILC tumors was defined as described above for ILC/ILC-like cell lines. Frequency of molecular alterations (MUT, MUT;LOH, MUT;GAIN, AMP, and DEL) in ILC and other clinically actionable breast cancer genes defined by ESCAT (ESMO Scale for Clinical Actionability of Molecular Targets) (6,57) were compared between tumors and cell lines. Enrichment of specific gene molecular alterations in tumors vs ILC/ILC-like cell lines was computed using fisher exact test. Key oncogenic pathways used in Supplementary Figure S12 were adapted from a previous study (58).

To evaluate *CDH1* alteration landscape in tumors and cell lines, we performed integrative analysis multi-omic datasets including RNA expression, RPPA, mutations and copy number. TCGA ILC and NST tumors datasets were acquired from cbioportal (3,55) and integrated breast cell line datasets generated above were analyzed together. RNA and RPPA values were row normalized in and cell lines datasets separately. Only truncating (non-sense, nonstop, frame shift and splice site mutations) and missense mutations were considered in this analysis. *CDH1* mutation lollipop plot was generated using protein paint webtool (https://proteinpaint.stjude.org/) (59). Enrichment of *CDH1* biallelic alterations (MUT+LOH and

Dual Loss) in ILC tumors and ILC/ILC cell lines vs NST tumors and NST cell lines was computed using fisher exact test.

E-cadherin and p120-catenin Immunofluorescence

ILC/ILC-like cell line immunofluorescent analysis using E-cadherin and p120-catenin was performed as described in our previous study (60). Briefly, cells were plated at a density of 100,000–200,000 cells/well on glass coverslips in 24-well plates, fixed on ice in ice-cold methanol for 30 minutes and blocked in blocking buffer (0.3% Triton X-100, 5% BSA, 1X DPBS) for 1 hour at room temperature. Primary antibody incubation was performed overnight at 4°C: Cell Signaling Technology E-cadherin (Cat # 3195) and BD Biosciences p120 catenin (Cat # 610134). Secondary antibody incubation was done for 1 hour at room temperature followed by Thermo Fisher Scientific Hoechst 33342 (Cat # 62249) staining. Coverslips were mounted with Polysciences Aqua-Poly/Mount (Cat # 18606–20) and images were taken on a Nikon A1 confocal microscope. This experiment was performed by Dr. Laura Savariau.

Aberrant DNA Methylation Events and Epigenetic Activation of *TFAP2B* Gene

To evaluate DNA methylation (DNAm) in breast cancer tumors, we utilized TCGA HM450K array dataset that was preprocessed using Sesame tool (46) by Silva et al in their recent publication (61). The DNAm instability (DMI) index per sample was computed by cumulative addition of DNAm deviations from control samples (tumor adjacent normal tissue). Briefly, DMI per sample was computed by adding all the differences between B-value of each

305 probe compared that probes mean B-value in tumor adjacent normals. The resulting DMI
306 scores were normalized against the tumor adjacent normals resulting in DMI z-scores.
307 To identify aberrant DNAm events in breast cancer tumors. Briefly, for each tumor the
308 methylation intensity i.e., B-values of probe were compared to its distribution in tumor
309 adjacent normal population. This allowed us to identify aberrantly methylated probes i.e.,
310 hyper- or hypo- methylated in tumor samples compared to normal samples. Hyper- and hypo-
311 methylated probe frequency was compared between luminal A ILC vs NST tumors to identify
312 aberrantly methylated probes in lobular disease (Figure 4C).
313 DNAm of all probes mapping to *TFAP2B* promoter region, defined as +/- 300bp of the
314 transcription start site (TSS), and their effect on *TFAP2B* gene expression was investigated using
315 Pearson correlation. Two probes mapping to *TFAP2B* gene TSS/exon 1 (cg25593948) and exon 2
316 (cg27260772) showed the strongest negative correlation with gene expression. Same probes
317 were evaluated in TCGA HM450 dataset. Differential methylation analysis of TCGA Luminal-A
318 ILC vs NST tumors using DNAm B-values was performed using R package Limma (62). Significant
319 differentially methylated probes were defined as effect size > 0.1 and adjusted p-value < 0.05.
320 These probes were mapped to genes using Infinium annotations (47). *TFAP2B* was the only
321 gene with the highest number of differentially methylated probes (N = 12) as shown in
322 Supplementary Figure S6B,C.

Identification of Functional Fusions

Putative fusions identified from OGM were further evaluated to see whether they had any gain or loss of expression of one or both fused genes. This resulted in fusions that had functional effects on the fused genes, hereafter referred to as functional fusions. Association of specific structural variation types (Del, Ins, Inv, Dup, Transloc-inter and Transloc-intra) and chromothripsis events with presence of functional fusions was computed using fisher exact test. Frequency of functional fusions in cell lines was compared those in tumor fusions using tumorfusion dataset (https://www.tumorfusions.org/) (63).

Differential Gene Dependencies

To identify gene dependencies in ILC/ILC-like cell lines we utilized Marcotte el al 2016 (Neel Lab) RNAi loss of function screen dataset. There was data available for the following 10 ILC/ILC-like cell lines; MDAMB330, MDAMB134VI, CAMA1, HCC2218, OCUBM, SKBR3, MDAMB453, 600MPE, HCC2185 and SUM44PE and 12 luminal NST cell lines (Figure 19A). To perform differential dependency analysis, we utilized a consensus approach where differential dependencies were identified using three different algorithms. The original RNAi comprised of zGARP values. Same RNAi dataset reprocessed using DEMETER2 was acquired from DepMap (DepMap: The Cancer Dependency Map Project at Broad Institute) (16). Both zGARP and DEMETER2 values underwent differential analysis using R package Limma (62). The final tool used for processing and differential analysis was R package siMEM (12) using default parameters. Consensus differential dependencies were curated from individual differential

analyses (p-value < 0.05) using zGARP, DEMETER2 and siMEM. Consensus differential dependencies showing higher dependency in ILC/ILC-like cell lines were defined as high dependency and vice versa as low dependency genes. Geneset enrichment of high and low dependency genes using hypergeometric test was performed using R package hypeR (64). Druggable dependencies were identified by queries high and low dependency genes in drug gene interaction database (dgidb.org/) (65).

Data Availability

All data generated in this study is available in the supplementary files and on our local cbioportal instance (https://cbioportal.crc.pitt.edu/).

Figures & Illustrations

Most bioinformatic analysis visualizations were generated using R packages ComplexHeatmap (66) and ggplot2 (67). Mutational lollipop plot was made using proteinpaint.stjude.org (59). These visualizations were aesthetically improved in power point to produce the final figures. Some illustrations including an overview of ICLE were prepared using BioRender.com.

Results

Multi-omic Characterization of ILC and ILC-like Cell Lines

We initiated the ILC cell line encyclopedia (ICLE) by collection of all available *CDH1*/E-cadherin or *CTNNA1*/α-catenin deficient ILC and ILC-like cell lines. Two ILC-like cell lines (SKBR5 and ESVA-T) were not publicly purchasable at the time of project initiation. The final ICLE cell line panel included a total of 17 cell lines including 8 ILC and 9 ILC-like cell lines (Supplementary Table S1). ICLE cell lines underwent molecular characterization using various multi-omics assays including optical genome mapping (OGM), whole-exome sequencing (WES), RNA sequencing (mRNAseq), reverse-phase protein array (RPPA), DNA methylation (DNAm) array and SNP array (Figure 1A and Supplementary Table S1). ICLE datasets were integrated with public datasets containing NST cell lines for downstream analyses (Supplementary Table S2). Comparison of genotype calls between ICLE and Marcotte et al (12) datasets showed strong similarity indicating that the same cell line variants were profiled in this and previously published datasets (Supplementary Figure S1).

Consensus clustering mRNA, RPPA and DNAm datasets revealed concordant molecular subtypes across three datatypes with mRNA subtypes being the most granular and refined (Figure 1B and Supplementary Figures S2, S3 and S4). Using mRNA subtyping, five ILC/ILC-like cell lines were categorized as Luminal (Lum), 9 as luminal/HER2 (Lum/HER2) and the remaining 3 were grouped into HER2, Basal and Claudin Low (Claudin/Low) subtypes (Figure 1B). Both mRNA subtypes and PAM50 based intrinsic molecular subtypes classified known ER+/luminal

378 cell lines (such as MDAMB134VI, BCK4, SUM44PE, CAMA1 and MDAMB330) as Luminal
379 (Supplementary Figure S2A,D). However, unlike mRNA subtyping, PAM50 based subtyping
380 failed to characterize SKBR3, a known HER2 cell line, correctly as the HER2-enriched subtype
381 (Supplementary Figure S2A,D). Indeed, PAM50 based molecular subtyping was developed for
382 tumor datasets (51,52) and may not be suitable for cell line datasets. Consensus clustering
383 based mRNA subtypes revealed cell lines (600MPE, UACC3133, HCC2185, WCRC25, IPH926,
384 HCC2218, ZR7530, OCUBM, MDAMB453) with both luminal and HER2 features by grouping
385 them into Lum/HER2 subtype. Since most ILC tumors are estrogen receptor alpha (ER-A)
386 positive and luminal in nature, the best models would be ER-A+/luminal ILC/ILC-like cell lines.
387 Most ILC/ILC-like cell lines were Lum or Lum/HER2 subtype (Figure 1B) and notably, several
388 Lum/HER2 ILC/ILC-like cell lines despite having low levels of ER-A/PR retained high expression
389 of ER target genes associated with ER+ tumors (i.e., ERpos gene signature) as well as had high
390 score for inferred sensitivity to endocrine therapy (Figure 1C; Supplementary Figure S2A).
391 Indeed, most (N = 14) ILC/ILC-like fell into luminal subtype in line with the observation that
392 most ILC tumors are of luminal subtype (3). Importantly, previous studies show that ILC cell
393 lines derived from ER+ ILC tumors (such as IPH926) may lose ER expression but retain their
394 luminal gene expression pattern (68).
395 Multi-omic features of profiled ILC/ILC-like cell lines are shown in Figure 1D and
396 Supplementary Table S1. All Lum cell lines showed high levels of ER-A and/or PR while low
397 levels of HER2/phospho-HER2 (except MDMAB330, a HER2/ERBB2 amplified cell line). Similarly,
398 Lum cell lines (except for MDAMB330) overall showed a lower frequency of structural
399 variations (SV), fusions and tumor mutational burden (TMB). On the other hand, Lum/HER2 cell

lines had low levels of ER-A/PR, but high levels of HER2/phosphor-HER2 (in cell lines with *HER2/ERBB2* mutations and amplifications). Moreover, they also had higher frequency of SVs, fusions and TMB with exception of WCRC25 which also showed lowest fraction of genome altered (FGA). Both OCUBM and MDAMB453 showed the highest TMB (>10 mutations per megabase) indicating a hypermutator phenotype. Non-luminal cell lines including SKBR3, HCC1187 and MDAMB468 lacked ER-A/PR and showed a higher frequency of SVs and high TMB. SKBR3 showed *ERBB2* amplification and consequently had higher levels HER2/phospho-HER2 while the other two cell lines lacked HER2 expression and were triple negative. All cell lines showed either *CDH1* or *CTNNA1* mutation as expected. Almost all showed *TP53* mutations or deletions except for BCK4 and ZR7530. Four cell lines showed alterations in *PIK3CA* and three in *PTEN* (both genes are components of oncogenic PI3K/AKT signaling) (58). Finally, only two cell lines had mutations in *BRCA2* including IPH926 (at 98% allele frequency indicating early event) and ZR7530 (at 32% allele frequency indicating later event in evolution).

Molecular Resemblance of Cell Lines to ILC Tumors

Breast cancers are driven by copy number alterations and major subtypes such as luminal, HER2 and basal subtypes each have distinct copy number profiles (3,69,70). Comparison of cell line copy number profiles to tumors provides a valuable tool for assessment of genome-wide molecular resemblance (12,71). Towards this goal, we compared copy number profiles of Lum, Lum/HER2 and non-luminal/Other ILC/ILC-like cell lines with those of tumors. As most ILC/ILC-like cell lines were derived from metastatic lesion or ascites fluids (8), we included comparison

with both primary and metastatic ILC tumors from TCGA (3) and MSK (54), respectively. Notably, both primary and metastatic ILC tumors showed very similar copy number profiles (Figure 1E) reminiscent of luminal tumors (70). Overall, Lum cell lines showed most similar copy number profiles to primary and metastatic ILC tumors followed by Lum/HER2 cell lines. Both Lum and Lum/HER2 subtype ILC/ILC-like cell lines showed high frequency of following chromosomal arm copy number alterations; 1p-, 1q+, 6p+, 8p+, 8q-, 11q-, 13p/q-, 16p+, 16q- (contains the *CDH1* gene), 17q+ and 18p/q- events. Three non-luminal subtype cell lines were grouped together into the "Other" subtype category. As expected, both MDAMB468 (basal subtype) and HCC1187 (claudinLow subtype) cell lines showed distinct copy number profiles and harbored 1p+ and 11p/q+ which were largely absent in other cell lines and tumors (72). On the other hand, SKBR3 (HER2 subtype) showed more resemblance to its luminal counterparts than its triple negative group members and harbored 1p-, 1q+,16q- and 18p/q-.

In addition to genome-wide copy number alterations, single nucleotide variations/alterations or mutations play a critical role in breast cancer initiation and progression. For example, *CDH1* mutations are very common in ILC tumors and involved in tumorigenesis (73,74), while *GATA3* and *MAP3K1* mutations are more frequent in tumors (3) (Supplementary Figure S5A). In line with the Knudson "two hit" hypothesis, tumor suppressor genes such as *CDH1* and *TP53* showed biallelic inactivation and harbored two molecular alterations e.g., truncating mutation in one allele and copy number loss of the second allele or loss of heterozygosity (LOH) (Supplementary Figure S5A,B). To further assess molecular resemblance of ILC/ILC-like cell lines to ILC tumors, we compared frequency of molecular alterations in key ILC genes and other clinically actionable genes between ILC/ILC-like cell lines

vs primary or metastatic ILC tumors (Figure 1F). To identify whether frequency of key alterations in ILC/ILC-like cell lines is similar or distinct from tumors we performed fisher's exact test. ILC/ILC-like cell lines retained molecular alterations at a similar frequency (fisher exact test non-significant) to primary and metastatic tumors in key ILC genes including *CDH1* (82% in cell lines vs 65% in primary tumors and 80% in metastatic tumors), *PTEN* (18% in cell lines vs 13% in primary tumors and 13% in metastatic tumors), *TBX3* (18% in cell lines vs 16% in primary tumors and 10% in metastatic tumors) and *FOXA1* (12% in cell lines vs 7% in primary tumors and 13% in metastatic tumors). In addition, ILC/ILC-like cell lines also retained similar frequency (fisher exact test non-significant) of molecular alterations in numerous other key breast cancer and clinically actionable genes including *PIK3CA* (24% in cell lines vs 49% in primary tumors and 45% in metastatic tumors), *CCND1* (29% in cell lines vs 17% in primary tumors and 20% in metastatic tumors) and *FGFR1* (18% in cell lines vs 9% in primary tumors and 3% in metastatic tumors). However, unlike tumors, ILC/ILC-like cell lines showed a higher frequency (and enrichment) of molecular alterations in the following genes; *TP53* (88% in cell lines vs 8% in primary tumors and 20% in metastatic tumors), *ERBB2* (47% in cell lines vs 11% in primary tumors and 13% in metastatic tumors), *BRIP1* (29% in cell lines vs 6% in primary tumors and 1% in metastatic tumors), *PPM1D* (35% in cell lines vs 5% in primary tumors and 2% in metastatic tumors), *NF1* (24% in cell lines vs 4% in primary tumors and 7% in metastatic tumors), and *ARID1B* (12% in cell lines vs 1% in primary tumors and 2% in metastatic tumors). Interestingly, several of these genes are found on chromosome 17 (*TP53* on 17p13.1, *ERBB2* on 17q12, *BRIP1* on 17q23, and *PPM1D* on 17q23). Both *BRIP1* and *PPM1D* were the same 17q23.2 locus and were co-amplified in all altered cell lines (Supplementary Figure S5B).

464 All ILC/ILC-like cell lines showed mutations in *CDH1* (E-cadherin) or *CTNNA1* (α-catenin)
465 (Figure 1D) and thus we hypothesized that these cell lines will have aberrant adherens junction
466 like ILC. To confirm, we performed immunofluorescence on 17 ILC/ILC-like cell lines
467 (Supplementary Figure S7). As expected, ILC/ILC-like cell lines, similar to ILC tumors, showed
468 aberrant adherens junctions defined by lack of membranous E-cadherin and/or cytoplasmic
469 p120 staining (Figure 2A). Some ILC/ILC-like cell lines, including OCUBM, MDAMB134VII,
470 HCC2218, SKBR3, HCC2185 and MDAMB468 did not harbor base pair mutations in the *CDH1* or
471 *CTNNA1* gene and yet showed aberrant adherens junctions. We comprehensively analyzed
472 molecular alterations in the *CDH1* and *CTNNA1* gene loci to understand the underpinnings of
473 this phenotype in these cell lines. Using optical genome mapping, we found that three of these
474 cell lines, HCC2185, HCC2218 and SKBR3, had large scale structural deletions in the *CDH1* gene
475 along with LOH (Figure 2B). Both MDAMB13VII and OCUBM had exonic deletions in the *CDH1*
476 genes along with LOH (Figure 2C) and MDAMB468 had a exonic deletion in the *CTNNA1* gene
477 (Figure 2C). Thus, DNA structural rearrangements in *CDH1* in ILC cell lines are common.
478 Notably, almost all *CDH1* mutations occurring in ILC tumors and ILC/ILC-like cell lines were
479 truncating in nature i.e., resulting in loss of E-cadherin protein, while *CDH1* mutations, which
480 were rarely seen in NST tumors and cell lines, were miss-sense in nature and did not affect E-
481 cadherin protein levels (Figure 2D). Moreover, all *CDH1* mutations in ILC/ILC-like cell lines had
482 near 100% allele frequency indicating these were clonal events that occurred early in evolution,
483 while those in NST cell lines, except CAL-148 which had a clonal silent mutation, occurred at
484 ~50% allele frequency indicating sub-clonal events that occurred later in evolution
485 (Supplementary Figure S5C). Overall, biallelic inactivation of *CDH1,* via either short variant plus

LOH (MUT+LOH) or large/exonic deletion plus LOH (Dual loss), was significantly enriched in both ILC vs NST tumors ($p < 0.0001$) and ILC/ILC-like vs NST cell lines ($p < 0.0001$) (Figure 2E). The multi-omic *CDH1* alterations landscape in breast cancer tumors and cell lines is illustrated shown in Figure 2F. Overall, ILC/ILC-like cell lines showed enrichment of both *CDH1* mutations, copy number loss, low mRNA and E-cadherin protein levels similar to like ILC tumors. Unlike ILC tumors and ILC/ILC-like cell lines, many NST tumors and cell lines showed *CDH1* copy number gains.

In summary, most ILC/ILC-like cell lines were of Lum or Lum/HER2 subtype and showed high activity of ERpos gene signature as well as high score for inferred sensitivity to endocrine therapy. Moreover, they showed similar copy number profiles to ILC tumors and retained molecular alterations in key ILC genes at similar frequency to tumors. Notably, most ILC/ILC-like cell lines recapitulated the *CDH1* alterations of ILC and showed concomitant disruption of adherens junctions.

Characterization of Whole-Genome Structural Variations, Chromothripsis Events and Functional Gene Fusions

DNA structural rearrangements and complex chromothripsis events have been largely uncharacterized in ILC/ILC-like cell lines. We performed optical genome mapping (OGM) of ILC/ILC-like cell lines (Figure 3A , Supplementary Figure S8). The most frequent type of structural rearrangement was deletions (Del, N = 1528), and least common was inversions (Inv, N = 166). However, if combined, intra-chromosomal and inter-chromosomal translocations

506 together were the most abundant (N = 1942) type of structural rearrangement. Overall, Lum
507 ILC/ILC-like cell lines (except for MDAMB330) had a lower frequency of structural
508 rearrangements than other subtypes with BCK4 having the fewest and SKBR3 (HER2 subtype)
509 having the highest structural rearrangements, indicating that Lum cell lines were genomically
510 more stable than Lum/HER2 and non-luminal cell lines (Figure 3A). Moreover, the frequency of
511 structural rearrangements showed significant correlation (R = 0.58, p = 0.03) with the frequency
512 of mutations or TMB (Supplementary Figure S9A) suggesting that genomically unstable cell lines
513 may have a higher frequency of both structural rearrangements and mutations. Moreover,
514 unlike in the case of mutations, where its frequency was strongly correlated (R=0.65, p =
515 0.00081) with chromosomal size i.e., more mutations were found in longer chromosomes such
516 as chromosome 1 (Supplementary Figure S9D,G), the frequency of structural variations did not
517 show significant correlation with chromosome size (R = 0.33, p = 0.13, Supplementary Figure
518 S9C,F). However, there was a much stronger yet imperfect correlation between frequency of
519 non-translocation structural rearrangements and chromosomal size (R = 0.5, p = 0.014,
520 Supplementary Figure S9E). This suggested that unlike mutations, structural rearrangements,
521 especially translocations may selectively occur in specific genomic locations and may not just
522 happen across the genome by chance.
523 Indeed, chromosomal translocation events most frequently involved chromosome 8 (359
524 Transloc-intra, 392 Transloc-inter), 11 (120 Transloc-intra, 145 Transloc-inter) and 17 (161
525 Transloc-intra, 216 Transloc-inter) compared to all other chromosomes which on average had
526 20 Transloc-intra/chromosome and 39 Transloc-inter/chromosome (Supplementary Figure S8
527 and Supplementary Figure S9C). Moreover, many of these translocation events appeared

528 clustered together and localized in nearby regions. This genomic instability is reminiscent of
529 chromothripsis which is characterized by large-scale structural rearrangements occurring
530 together and localized to isolated chromosomal regions that harbor oscillatory changes in copy
531 number (44).

532 To comprehensively characterize these complex events, we employed an algorithm
533 shatterseek that identifies chromothripsis events by detecting intra-chromosomal
534 translocations occurring in interleaved fashion and are accompanied by oscillatory copy number
535 changes (44). We identified high and low confidence chromothripsis events across most cell
536 lines except for BCK4, CAMA1 and UACC3133 (Figure 3B and Supplementary Figure S8). High
537 confidence chromothripsis events across cell lines were most frequent in chromosomes 8 (in 5
538 cell lines), 17 (4 cell lines) and 6/11/13 (2 cell lines each). Indeed, these findings are in line with
539 previous reports showing that breast cancers have distinct chromothripsis patterns involving
540 chromosomes 8, 11, and 17 (75,76).

541 Next, we identified N = 384 functional fusions from N = 525 putative fusions by selecting
542 those that resulted in gain (N = 302) or loss (N = 82) of expression of its fusion partners
543 (Supplementary Figure S10A). Like tumors, most functional fusions identified in ILC/ILC-like cell
544 lines involved genes residing in chromosome 8 (N = 64 fusions), 11 (N = 63 fusions) and 17 (N =
545 89 fusions) (Figure 3D). Most of these functional fusions were gain of expression fusions (GEFs)
546 which mostly resulted from structural rearrangements occurring in these three chromosomes
547 (Figure 3C) and were strongly associated (fisher exact test, p = 0.0082) with inter-chromosomal
548 translocation events. Moreover, GEFs also showed strong enrichment (fisher exact test, p =
549 0.029) in cell lines with chromosome 17 chromothripsis. On the other hand, loss of expression

(LEFs) fusions involved genes residing on chromosome 1 (N = 10), 8 (N = 7) and 12 (N = 7) and were significantly associated with deletions events (fisher exact test, p = 0.0001). Most common genes involved in fusions included *SHANK2* and *TENM4* on chromosome 11 and *BCAS3*, *GRB7*, *PPM1D* and *SKAP1* on chromosome 17 (Supplementary Figure S10B,C).

In summary, using OGM, we unveiled the whole-genome structural rearrangement landscape of ILC/ILC-like cell lines and characterized chromothripsis events and functional gene fusions.

Aberrant DNA Methylation Events and Epigenetic Activation of *TFAP2B*

DNA methylation (DNAm) changes have been associated with breast cancer risk (77–79) and have been shown to be very different in distinct molecular subtypes of breast cancer (80,81). Moreover, identification of DNAm changes associated with distinct disease can reveal novel biomarkers for early detection and treatment response prediction (82,83). However, DNAm changes associated with lobular breast cancer remain largely unexplored. Towards achieving this goal, we sought to explore DNAm in breast cancer lines and tumors towards identifying novel biomarkers of lobular disease.

Our initial exploration of DNAm profiles of breast cancer cell lines revealed, as expected, that breast cancer cell lines cluster by their DNAm molecular subtypes (Supplementary Figure S4A,B). Notably, the DNAm subtypes closely resembled the mRNA subtypes (Supplementary Figure S4D). Next, we sought to quantify DNAm changes in cell lines vs. tumors by defining a DNAm instability index (DMI) which represents cumulative changes in DNAm across the

genome in cancer vs. normal samples. We found that overall breast cancer cell lines showed more aberrant DNAm (high DMI) than tumors (Supplementary Figure S4E,F). Higher DMI in cell lines in part maybe driven by culture condition induced epigenetic changes (84,85).

Next, we specifically examined non-basal cell lines to better delineate the differences between NST and ILC histology. Clustering of non-basal cell lines by the top variable DNAm B-values revealed that most ILC and ILC-like cell lines clustered separately from NST cell lines (Figure 4A). In contrast, clustering of luminal ILC and NST tumors by the top variable DNAm B-value revealed only partial separation of ILC and NST sample clusters (Figure 4B). To identify the top aberrantly methylated regions in NST vs. ILC tumors, we first identified non-variable methylated probes in normal samples and then assessed whether these probes were aberrantly methylated (i.e., hyper- or hypo- methylated) in tumor samples compared to normal samples. The top aberrantly methylated probes and the associated genes in ILC vs. NST tumors are shown in Figure 4C. The top aberrantly methylated probes and their associated genes in ILC included *TFAP2B, SCD, TAPBL* and *FOXN1*, while those in NST included *CCND1, PML, NSMCE1, NELFA*, *AQP7* and *RBPJL*. Notably, *TFAP2B* also came as the top hit in differential methylation analysis of in Luminal ILC vs NST tumors (Supplementary Figure S6B).

The *TFAP2B* gene encodes AP-2B, a novel mammary epithelial differentiation marker, which is preferentially expressed in ~80% of ILC tumors (86–88). In vitro studies indicate that AP-2B controls tumor cell proliferation of ILC/ILC-like cell lines (87). AP-2B positivity is associated with overall favorable clinicopathological characteristics and prolonged relapse-free survival (88,89). Integrative analysis revealed a pattern of hypomethylation of the *TFAP2B* gene and increased expression (Figure 4D) in both breast cancer tumors and cell lines. *TFAP2B*

epigenetic activation and its concomitant high expression were particularly observed in ILC tumors and ILC/ILC-like cell lines with exception of two ILC (MDAMB330 and SUM44PE) and four ILC-like (HCC2218, CAMA1, HCC1187 and MDAMB468) (Supplementary Figure S6A). There was a strong negative Pearson correlation between *TFAP2B* gene expression and promoter/exon 1 probe methylation in breast cancer tumors and cell lines is shown in Figure 4E. Genomic alterations in *TFAP2B* were rare and were only seen in one ILC (amplification in UACC3133) and two NST (mutation in BT483 and CAL851) cell lines.

In summary, we explored the DNAm landscape of breast cancer tumors and cell lines and performed systematic and integrative analysis of breast cancer cell lines and tumor methylation datasets to reveal epigenetic activation of *TFAP2B*, an important emerging biomarker of lobular disease, in both ILC/ILC-like cell lines and ILC tumors.

Cataloguing Gene Dependencies and Identifying Druggable Vulnerabilities

CDH1 molecular alterations and E-cadherin deficiency is an attractive target for development of precision therapies for ILC. Several molecular studies have shown evidence that E-cadherin deficient cell lines have several druggable vulnerabilities including but not limited to GPCR signaling (90,91), PI3K/AKT and IGF1R pathway (90,92), and synthetic lethality with ROS1 inhibition (91,93). These studies have led to a currently ongoing precision medicine trial for ILC called ROSALINE which is investigating efficacy of ROS1 inhibitors in early setting of ER+ ILC disease (94). Despite these recent findings, a major bottleneck in comprehensive investigation of targeted therapies in ILC is lack of suitable preclinical models. Indeed, most of the

aforementioned studies and their findings are based on modeling E-cadherin defects in genetically modified cell lines and lack ILC context.

To overcome these limitations, we sought to identify genes that show higher dependency (i.e., essential for survival) in ILC/ILC-like cell lines vs NST cell lines. For this we employed publicly available RNAi loss of function screen datasets from Marcotte et al (12). To avoid contamination by subtype specific differences, we restricted our analysis to luminal cell lines. We identified differential dependencies between 10 ILC/ILC-like vs 12 NST cell lines using RNAi datasets processed via three different algorithms to improve robustness of our findings (Figure 5A). Concordant differential dependencies across three algorithms were used to define consensus differential dependencies which included 98 high and 94 low dependency genes in ILC/ILC-like vs NST cell lines (Figure 5B). Over-representation analysis using KEGG database revealed that high dependency genes were associated with actin cytoskeleton, focal adhesion pathways and mTOR signaling, while low dependency genes were associated with cellular senescence and insulin signaling (Figure 5C). Both low dependency genes associated pathways were also identified in ingenuity pathway analysis (Supplementary Figure S11A,B). Select high dependency genes in the actin cytoskeleton, focal adhesion and PI3K/AKT/mTOR signaling are shown in Figure 5D. Both *PPP1R12B* and *ITGA11* genes were involved in more than one pathway. Next, we identified druggable gene dependencies by querying the identified gene dependencies (Figure 5B) in the drug gene interaction database. This resulted in shortlisting of 17 high and 17 low dependency genes that were druggable and had targeted drugs against them (Figure 5E). Several of these druggable high dependency genes were components of actin

633 cytoskeleton (*CHRM4*), Focal adhesion (*PDPK1*), PI3K/AKT/mTOR signaling (*STK11*, *CCNE1*,
634 *PDPK1*).
635 In summary, our differential dependency analysis revealed numerous druggable
636 vulnerabilities in ILC/ILC-like cell lines that hold potential to develop novel precision therapies
637 for E-cadherin deficient breast cancers.

638 **Scheme for Rational Selection of ILC/ILC-like Cell Lines for Modelling ILC**

639 ILC focused studies have majorly relied on a small subset of ILC/ILC-like cell lines for
640 modeling this disease (Supplementary Table S1, see column of ILC focused PubMed reports).
641 We sought to expand the list of suitable ILC/ILC-like cell lines available for modeling
642 ER+/Luminal ILC disease by proposing a scheme for rational selection of these cell lines,
643 summarizing their key multi-omic features considering this scheme and recommending suitable
644 models.
645 The proposed scheme for rational selection of ILC/ILC-like cell lines and their key multi-
646 omic features cell lines are summarized in Figure 6. This qualitative scheme is based on three
647 criteria; 1) molecular subtype, 2) molecular alterations and 3) deregulated/altered pathways
648 (Figure 6A). Breast cancer cell lines to model specific types of breast cancers are selected based
649 on their molecular subtype. Since most ILC tumors are ER+ and luminal in nature, the best
650 models would be ER+/luminal ILC/ILC-like cell line. Most ILC/ILC-like cell lines were Lum or
651 Lum/HER2 subtype (Figure 6B) and notably, several Lum/HER2 ILC/ILC-like cell lines despite
652 having low levels of ER-A/PR retained high expression of ER associated genes as shown by

653 ERpos gene signature scores (Figure 1C; Supplementary Figure S2A). Hence, overall, most
654 luminal ILC/ILC-like cell lines would serve as useful models to study ER+/Luminal disease based
655 on this criterion. On the other hand, non-luminal ILC/ILC-like cell lines such as HCC1187
656 (ClaudinLow), MDAMB468 (Basal) and SKBR3 (HER2) are not good models for ER+/luminal ILC
657 disease but maybe useful for studying rare types of non-luminal ILC with similar molecular
658 subtype or studying *CDH1* or *CTNNA1* defects in non-luminal breast cancers.

659 Next, it is important to select ILC/ILC-like cell lines based on their genetic context. Based
660 on our initial selection, only ILC/ILC-like cell lines with alterations in *CDH1* or *CTNNA1* genes
661 were selected. In addition to the ILC pathognomonic alterations, several cell lines also had
662 molecular alterations in less frequently altered genes like *PTEN* (CAMA1, MDAMB453 and
663 MDAMB468) and *FOXA1* (SUM44PE and MDAMB453). However, only 8% of ILC tumors have
664 *TP53* molecular alterations, these very present in almost all ILC/ILC-like cell lines except BCK4
665 and ZR7530, making them suitable models to study *TP53* WT ILC tumors. Conversely, most
666 (49%) of the ILC tumors have *PIK3CA* molecular alterations, but these were less frequent in
667 ILC/ILC-like cell lines (which included BCK4, MDAMB453, OCUBM and HCC2185). Moreover, two
668 ILC/ILC-like cell lines (CAMA1 and MDAMB453) had molecular alterations in *PTEN*, both this
669 gene and *PIK3CA* are components of *PI3K/AKT* pathway, one of the most altered pathways in
670 ILC tumors (3,58).

671 The final criterion for rational selection is based on deregulated pathways. Often non-
672 recurrent alterations may occur in multiple different components of the same oncogenic
673 pathway resulting in its deregulation. Frequently deregulated oncogenic pathways that are
674 druggable in breast cancer include growth factor and receptor tyrosine kinase (RTK) signaling,

675 cell cycle and *TP53* pathway and DNA damage repair (DDR) pathway (3,58). Apart from these
676 genomically altered pathways, hormone (ER/PR) signaling is also an important breast cancer
677 pathway that primarily gets deregulated by increase in estrogen hormone levels (95). Most of
678 the luminal ILC/ILC-like cell lines showed higher expression of ERpos gene signature and lacked
679 expression of ERneg gene signature indicative of active hormone signaling. In line with these
680 findings, these cell lines also showed higher predicted sensitivity to endocrine therapy (Figure
681 1C). These findings reveal additional models (such as UACC3133, ZR7530, HCC2218,
682 MDAMB453, WCRC25, and IPH926) to study endocrine response and resistance in ILC.
683 Furthermore, all ILC/ILC-like cell lines had alterations in at least one of key oncogenic breast
684 cancer pathways (Supplementary Figure S12). The RTK pathway was altered in all ILC/ILC-like
685 most frequently due to alterations in *ERBB2* and *NF1* gene. Cell cycle pathway was altered in all
686 Lum ILC/ILC-like cell lines due to *CCND1* amplifications and *CDKN2B* mutation. While DDR and
687 PI3K pathways were altered frequently in Lum/HER2 cell lines. With this information,
688 researchers can choose suitable ILC/ILC-like cell lines based on the deregulated pathway on
689 interest. Notably, each of these pathways is druggable using systematic or targeted agents e.g.,
690 endocrine therapies to against hormone signaling, HER2 and PI3K inhibitors against RTK
691 signaling (96,97), chemotherapy and CDK4/6 inhibitors (54) for inhibiting cell cycle and
692 proliferation and PARP inhibitors against tumors with homologous repair defects (HRD) (98).
693 Knowledge of these deregulated pathways in ILC/ILC-like cell lines will be critical for developing
694 precision therapies for ILC.
695 Finally, in addition to the aforementioned qualitative criterions for choosing ILC/ILC-like
696 cell lines, we also defined quantitative scores for molecular similarity of cell line to ER+ ILC

tumors to aid in their selection. The molecular similarity of each ILC/ILC-like cell lines to ER+ ILC tumors was computed using Pearson correlation of their genome-wide copy number profiles and RNA expression. BCK4 showed the highest copy number and RNA similarity to ILC tumors. Most cell lines showed high copy number similarity except for MDAMB468. On the other hand, as expected, all non-luminal (MDAMB468, SKBR3, HCC1187) and few luminal (CAMA1, HCC2185 and OCUMB) showed low or non-significant RNA similarity to ILC tumors. Suitability of each cell line to model ER+/luminal ILC disease based on their molecular subtypes and molecular (copy number and RNA) similarity is summarized in Figure 6B.

Discussion

Despite ILC being acknowledged as a disease with distinct biology that necessitates specialized and precision medicine treatments, the further exploration of its molecular alterations with the goal of discovering new treatments has been hindered due to the scarcity of well-characterized cell line models (8,9). Previous large-scale cancer cell line characterization studies such as CCLE 2019 (11) and Sanger 2016 (13) had limited inclusion, and lacked comprehensive characterization, of ILC/ILC-like cell lines.

To address this gap, we generated the ILC Cell Line Encyclopedia (ICLE), providing the first comprehensive molecular characterization of ILC and ILC-like cell lines using state-of-the-art multi-omics comprising optical genome mapping, whole-exome sequencing, RNA sequencing, RPPA, SNP array and DNA methylation array. Our approaches were chosen in line with those used in previous large-scale cancer cell line characterization studies (11,12). This allowed us to integrate ICLE datatypes with corresponding published breast cancer cell line multi-omics datasets from Ghandi et al 2019 (11), Marcotte et al 2016 (12) and Iorio et al 2016 (13,15). and perform integrative and comparative (ILC vs NST) analyses.

As expected, all the ILC/ILC-like cell lines harbored molecular alterations in *CDH1*/E-cadherin and *CTNNA1*/α-catenin and showed disrupted adherens junctions, a hallmark of ILC phenotype. Moreover, consensus molecular subtyping not only confirmed the luminal status of well-established ILC cell lines (MDAMB134VI, MDAMB330, SUM44PE and BCK4) but also revealed additional cell lines that retained luminal molecular features despite the loss of ER-A/PR expression in some cases (IPH926, HCC2185, WCRC25, HCC2218, MDAMB453 and

OCUBM) thus expanding the list of luminal models. However, it is important to note that many of these cell lines also showed high HER2/phospho-HER2 expression (several due to HER2/ERBB2 amplifications) and were classified as Lum/HER2 subtype. Notably, despite this feature, most Lum/HER2 ILC/ILC-like cell lines showed high predicted sensitivity to endocrine therapy. Thus, in addition to the well-established ER+/Lum cell lines, these Lum/HER2 cell lines could also serve as promising models to study molecular mechanism of ILC drug resistance to endocrine therapies, a key ILC challenge (1,3,7,8,24,99–101).

Comparison of cell line molecular features to rumors revealed that most Lum and Lum/HER2 cell lines showed RNA and copy number similarity to tumors. Similarly, ILC/ILC-like cell lines retained molecular alterations in key ILC genes at similar frequency to both primary and metastatic ILC tumors. Notably, ILC/ILC-like cell lines recapitulated the *CDH1* alteration landscape of ILC tumors. Like ILC tumors, all *CDH1* mutant ILC/ILC-like cell lines had a truncating mutation along with LOH (key mechanism of biallelic inactivation of *CDH1* gene). Interestingly, we also identified novel *CDH1* large-scale structural deletions using OGM in three ILC/ILC-like cell lines as well as exonic deletions in two ILC/ILC-like cell lines, in both cases along with LOH. Notably, all *CDH1* mutations in ILC/ILC-like cell lines were clonal (100% allele frequency), i.e., acquired early in evolution, and seemed unlikely to have acquired in culture. Converse to these similarities, ILC/ILC-like cell lines showed enrichment of molecular alterations in *TP53*, *ERBB2* and several DNA repair genes (*BRIP1*, *PPM1D* and *DDX5*) which were significantly less frequent in ILC tumors.

Recent studies show that structural variations and complex genomic rearrangements are frequently seen in breast cancer genomes (75,76,102). However, whole-genome structural

variations and complex events such as chromothripsis have been largely uncharacterized in ILC/ILC-like cell lines. Using OGM, we found that ILC/ILC-like cell lines showed varying degrees of genomic instability ranging from very complex genomes with frequent structural rearrangements to others (mostly Lum cell lines) with relatively silent genomes with few structural rearrangements. Notably, we identified frequent chromothripsis events in chromosomes 8, 11 and 17 across ILC/ILC-like cell lines. These patterns of chromothripsis were breast cancer specific in line with previous reports (44,75,76). Interestingly, we also saw enrichment of gain of expression fusions on these same chromosomes implicating chromothripsis events as drivers of these functional fusions (44,75,76). Indeed, chromosome 17 contains many important breast cancer genes such as *TP53*, *ERBB2*, *NF1*, *BRCA1*, *MAP2K4*, *PPM1D*, *BRIP1* among others and single catastrophic events like chromothripsis affect large regions (containing various oncogenes and tumor suppressors) providing tumors with opportunities for rapid genome evolution (44,103,104).

TFAPAB gene is an emerging biomarker of lobular disease that is preferentially expressed in both precursor and invasive stages (87,88). Importantly, it controls differentiation and proliferation of tumor cells and has potential to serve as prognostic biomarker or a targetable vulnerability in ILC disease (105,106). Using integrative analysis of DNAm and RNA expression, we revealed epigenetic activation of *TFAP2B* gene in both ILC/ILC-like breast cancer cell lines and ILC tumors. This is an important finding that raises questions about whether E-cadherin defects reprogram epigenetic landscape of tumors cells resulting epigenetic activation of proliferation regulators such as *TFAP2B*. Additional studies are warranted to test this hypothesis and further investigate the role of *TFAP2B* in E-cadherin defective breast cancers.

E-cadherin deficiency is an attractive target for development of precision therapies for ILC (90,91,93). Towards the goal of identifying novel druggable vulnerabilities or dependencies associated with ILC, we analyzed publicly available RNAi loss of function breast cancer cell line datasets. In line with previous findings, we also observed that ILC/ILC-like cell lines have high dependency genes in cytoskeletal components and PI3K/AKT pathway (90,91) further confirming the significance of these pathways as putative vulnerabilities for ILC. In addition, we also uncovered novel dependencies in Focal adhesion and various metabolism related pathways related with tyrosine, vitamin B6 and retinoic acid metabolism. Importantly, this is the most comprehensive report on identification of novel druggable vulnerabilities using luminal ILC/ILC-like cell lines and overcomes limitations of previous studies, that due to lack of suitable models, had employed either genetically modified models or basal subtype E-cadherin deficient models to identify druggable vulnerabilities and lacked ILC context.

In summary, we performed comprehensive multi-omic profiling of E-cadherin deficient (ILC/ILC-like) cell lines and highlight their key molecular features including molecular subtypes and genomic alterations, evaluate their similarity to E-cadherin deficient (ILC) breast cancers, catalogue druggable vulnerabilities and finally present a scheme for rational-model-selection. The findings of this study expand the array of suitable cell lines available for modeling ILC and lay foundation for studying key ILC challenges including development of precision therapies and novel biomarkers as well as for generating novel hypothesis for future ILC research.

Acknowledgements and Funding

The work was in part supported by the Breast Cancer Research Fund (to SO and AVL) and NCI R01 CA252378 (SO/AVL) and P30CA047904. AVL and SO are Komen Scholars and Hillman Foundation Fellows. This research was also supported in part by the University of Pittsburgh Center for Research Computing, RRID:SCR_022735, through the resources provided. Specifically, this work used the HTC cluster, which is supported by NIH award number S10OD028483. Partial support was provided by the Magee-Womens Research Institute and Foundation and the Shear Family Foundation. We are also thankful to Jian Chen and Beth Knapick for outstanding technical support. Thanks to the University of Pittsburgh Genomic Research Core (GRC) and UPMC Genome Center for assistance in DNA/RNA sequencing and Illumina SNP array analysis. We would like to also thank Bionano for collaboration and assistance with optical genome mapping.

Figure Legends

Figure 1. Multi-omic Characterization of ILC and ILC-like Cell Lines and Molecular Resemblance to ILC.
(A) Overview of multi-omic profiling of 17 ILC and ILC-like cell lines using genomic (optical mapping, SNP array, whole-exome sequencing), epigenomic (DNA methylation array), transcriptomic (RNA sequencing) and proteomic (RPPA). **(B)** Multi-omic molecular subtypyes and their relationship with each other across each cell line. These subtypes were defined consensus clustering of mRNA, RPPA and DNA methylation (DNAm) datasets resulting in five mRNA subtypes (Luminal – Lum, Lum/HER2, Basal and CluadinLow), four RPPA subtypes (Lum, Lum/HER2, HER2, and Basal) and three DNAm subtypes (Lum/HER2, HER2, Basal, ClaudinLow/EMT and N/A for missing data on SKBR-3). **(C)** Hormone signaling activity and sensitivity to endocrine therapy (SET) in ILC/ILC-like cell lines. ERpos and ERneg gene signatures represent genes strongly associated with ER+ and ER- tumors, respectively. SET is defined as difference between mean of expression of ERpos and ERneg genes. **(D)** Overview of multi-omic features 17 cell lines clustered by mRNA subtypes. First panel highlights genomic metrics including fraction genome altered (FGA), structural variation (SV) count, fusion count and tumor mutation burden (TMB) and their values visualized as barplots. Second panel shows molecular alterations including two ILC driver alterations (CDH1 and CTNNA1) and other key ESCAT clinically actionable alterations. Third panel shows protein and levels of three receptors including ER-alpha (ER-A), PR, HER2 and phospho-protein levels of phosphorylated HER2-PY1248. Fourth, fifth and sixth panel show top variable multi-omic features including RNA (N = 5000), protein (N = 50) and DNAm (N = 5000). **(E)** Genome-wide linear plots showing copy number event frequencies across chromosomes in 1) N = 127 primary ILC tumors from TCGA, 2) N = 202 metastatic ILC tumors from MSK cohorts, 3) Luminal ILC/ILC-like cell lines, 4) Lum/HER2 ILC/ILC-like cell lines and 5) Other ILC/ILC-like cell lines. Copy gains are shown in red and copy loses in blue. Linear copy number plot of each cell line groups is followed by individual copy number plots of each cell line within that group. Key copy number alterations in tumors are listed below primary tumor copy number plot. **(F)** Barplot showing frequency of molecular alterations (mutations, amplifications and deletions) in various ILC associated genes and other clinically actionable breast cancer genes in primry ILC tumors vs ILC/ILC-like cell lines (left) and metastatic ILC tumors vs ILC/ILC-like cell lines (right). ILC associated genes include *CDH1*, *PTEN*, *TBX3* and *FOXA1* and others are clinically actionable breast cancer genes (defined by ESCAT – ESMO Scale for Clinical Actionability of molecular Targets). Fisher exact test was used to assess differences in frequency between comparison groups. All significant ($p <= 0.05$) differences are annotated while rest were non-significant.

Figure 2. ILC and ILC-like Cell Lines Recapitulate *CDH1* Alteration Landscape of ILC.

(A) P120 and E-cadherin immunofluorescence of ILC/ILC-like cell lines including MDAMB134VI (ILC cell line harboring LOH + *CDH1* exonic deletion), CAMA1 (ILC-like cell line harboring *CDH1* mutation at 100% allele frequency) and MDAMB330 (a *CDH1* WT ILC cell line harboring *CTNNA1* mutation at 100% allele frequency) vs one representative *CDH1* WT NST cell lines (MCF7). **(B)** Novel structural variations resulting in *CDH1* deletions identified using optical genomic mapping in HCC2185, HCC2218 and SKBR3. **(C)** Exonic deletions identified in *CDH1* (E-cadherin) and *CTNNA1* (alpha-catenin) genes using WES dataset. Red tiles show exonic deletions. **(D)** Lollipop plot (generated using proteinpaint.stjude.org) showing truncating (black) and missense (blue) mutations across *CDH1* gene (including exons that form amino acid sequence and annotated with associated domains) in TCGA tumors (left) and ICLE/CCLE cell lines (right). The exon boundaries are shown by dotted lines, the numbers in each segment represent amino acid/protein length and the length of the lollipop represents the frequency of each mutation. **(E)** Barplots showing alteration frequency of *CDH1* gene in TCGA ILC vs NST tumors and ICLE ILC/ILC-like vs CCLE NST cell lines. Alterations are categorized as absence of alteration or wild-type (WT), mutation only (MUT Only), single allele copy number loss only (loss of heterozygosity – LOH Only), single allele copy number gain (GAIN), Mutation + LOH (MUT + LOH), and LOH plus exonic deletions or large structural deletions (Dual Loss). Association of *CDH1* biallelic inactivation in ILC vs NST tumors and cell lines was tested using fishers exact test (p-value < 0.0001, ****). **(F)** Heatmaps showing *CDH1* mutations, mRNA levels, copy number and protein levels in tumors (TCGA 127 ILC vs 489 NST) (left) and cell lines (ICLE 17 ILC and ILC-like vs CCLE 39 NST cell lines) (right).

Figure 3. Optical Genome Mapping Unveils Structural Variations, Chromothripsis Events and Functional Gene Fusions. **(A)** Overview of structural variation types and their frequency across cell lines along with other metrics of genomic instability (TMB, FGA and # of fusions). SV types include deletions (del), duplications (dup), insertions (ins), inversions (inv), inter-chromosomal translocations (transloc-inter) and intra-chromosomal translocations (transloc-intra). **(B)** Heatmap (left) shows overview of chromosomal chromothripsis events predicted by shatterseek algorithm across cell lines. High and low confidence events are shown in yellow and green respectively. Circos plots (right) show SVs, CNVs and chromothripsis events in HCC2185 (ILC) and ZR750 (ILC-like) cell line. Details of each track are shown in supplementary figure 8. Briefly, track 1 hg19 cytoband, track 2 chromothripsis regions, track 3 SV track (excluding translocations), track 4 CNV track, track 5 gene annotations and track 6 translocations. **(C)** Shows circos plots highlighting translocation events in chromosome 8, 11 and 17 and chromosome 1, 8 and 12 resulting in gain of expression fusions (GEFs) and loss of expression fusions (LEFs), respectively. Only breast cancer driver genes involved in these gene fusions are shown. **(D)** Barplot showing frequency of fusion events across all chromosomes in ICLE (left) and Tumors as reported in tumorfusions database (right). Chromosomes are ordered by decreasing order of fusion frequency with highest frequency of fusions in the chromosome 17 (left) and 15 (right).

Figure 4. Aberrant DNA Methylation Events and Epigenetic Activation of TFAP2B.

871 **(A)** Heatmap showing cell line – cell line similarity based on clustering using top 10% variable DNAm features
872 across non-basal ILC/ILC-like and NST cell lines. **(B)** Heatmap showing sample – sample similarity based on
873 clustering using top 10% variable DNAm features across TCGA luminal ILC and NST tumors. **(C)** Top aberrantly
874 methylated probes and associated genes in TCGA luminal ILC vs NST tumors. Type of probe includes highDNAm
875 (high DNAm in normal samples), midDNAm (mid DNAm in normal samples) and lowDNAm (low DNAm in normal
876 samples). **(D)** Heatmaps showing regulation of *TFAP2B* gene expression via DNA methylation of probes mapping to
877 its transcription start site (TSS)/Exon 1 (cg25593948) and Exon 2 (cg27260772) in both tumors (left) and cell lines
878 (right). TFAP2B gene illustration shows its seven exons and location TSS. Tumors and cell lines are annotated by
879 histology (ILC, NST and ILC-like) and intrinsic molecular subtypes (PAM50 for tumors and mRNA subtypes for cell
880 lines). Probes are annotated by the region they map to and their Pearson correlation (cor) of DNA methylation
881 levels with *TFAP2B* gene expression. **(E)** Scatter plots showing correlation between cg25593948 probe DNA
882 methylation levels (B-value) with *TFAP2B* gene expression in tumors (left) and cell lines (right). The Pearson
883 correlation coefficient (R) and p-value (p) are shown in each scatter plot.
884

885 **Figure 5. Identification of Differential Gene Dependencies in ILC/ILC-like vs NST Cell Lines.**
886 **(A)** Scheme of differential dependency analysis to identify ILC/ILC-like specific gene dependencies compared to
887 NST cell lines. In total 10 ILC/ILC-like and 12 NST cell lines were selected with RNAi loss of function (LOF) screen
888 data from Marcotte et al study (Neel Lab). Three differential analyses were performed using RNAi LOF screen
889 dataset processed by three different algorithms (DEMETER2, zGARP and SIMEM). The overlapping findings from
890 each differential analysis were used to define consensus differential dependencies. **(B)** Heatmap showing 98 high
891 dependency genes and 94 low dependency genes identified from consensus differential dependencies in ILC/ILC-
892 like vs NST cell lines identified. Differential dependency log2FC and log-pvalue from SIMEM algorithm are shown in
893 left panels of the Heatmap. **(C)** Barplots showing KEGG pathways enriched in high (left) and low (right) dependency
894 genesets identified in panel B. Enriched was computed using hypergeometric test. Barplot x-axis shows -log10 of p-
895 value from hypergeometric test. **(D)** Key high dependency pathways and associated genes along with their log fold
896 change (logFC) in the tables above and dependency scores in ILC/ILC-like vs NST cell lines in the heatmaps below.
897 **(E)** Heatmap showing druggable high and low dependency genes identified by overlapping genes in panel B with
898 druggable genes reported in drug gene interaction database (https://www.dgidb.org/) along with their reported
899 druggability score (drug score). A higher score indicates strong literature evidence (# of reports) for a particular
900 gene to be druggable/targetable by a specific drug.

Supplementary Tables Figures

Supplementary Table S1. Overview of ICLE Cell line Panel and Their Key Multi-omic Features.
All PubMed reports on each cell line, only ILC focused pubmed reports on each cell line, Type (ILC or ILC-like), receptor Subtypes defined based on protein expression of ER, PR, HER2, and phosphorylated- HER2 protein levels in RPPA dataset. Molecular Subtypes include PAM50 based subtypes, mRNA subtypes, RPPA subtypes and DNAm subtypes. Molecular Alterations in ILC Drivers Genes. Finally, genome-wide metrics include fraction of genome altered (FGA), tumor mutation burden (TMB), structural variation count (SV), and chromothripsis events.

Supplementary Table S2. Overview of the Generated ICLE Datasets.
Columns show data types, technology used to generate the data and data levels for all 17 ILC/ILC-like cell lines.

Supplementary Table S3. Overview of Public Datasets Used for Intergration.
Columns show ICLE datasets and corresponding public datasets used for intergration across each datatype.

Supplementary Figure S1. Genotype Similarity between ICLE and Marcotte et al (Neel Lab) Datasets.
Five thousand randomly selected SNP calls were compared between all cell lines to assess genotyping similarity (percentage of overlapping SNP calls divided by total SNP calls – 100% means high similarity while 0% means no similarity). Overlapping cell lines are shown in red, while ICLE cell lines with no match in Marcotte dataset are shown in blue.

Supplementary Figure S2. Exploration of RNA Sequencing Dataset and Defining mRNA Subtypes.
(A) Consensus clustering was performed on row normalized expression matrix where features represent top 5000 variable features (identified using mean absolute deviation (MAD). K = 9 was used to define refined clusters. Final mRNA subtypes based molecular features of cell lines including E-cadherin, ER, HER2 and Claudin-7 protein levels, ERpos gene signature scores and PAM50 based intrinsic molecular subtypes. Few clusters showing similar molecular features were combined to result in biologically meaningful mRNA subtypes. **(B)** PCA plot and **(C)** expression heatmap generated using top variable features show to see transcriptic relationship between distinct mRNA subtypes. **(D)** Sankey diagram showing relationship between cell line PAM50 calls and mRNA subtypes

Supplementary Figure S3. Exploration of RPPA Dataset and Defining RPPA Subtypes.

(A) RPPA subtypes defined by consensus clustering of top 50 varibale features defined by MAD as described before. K = 9 was used like before and then based on molecular similarity some clusters were combined to result in 6 clusters. **(B)** PCA plot and **(C)** RPPA expression heatmap generated using top variable features show to see proteomic relationship between distinct RPPA subtypes. **(D)** Sankey diagram showing relationship between cell line mRNA and RPPA subtypes.

Supplementary Figure S4. Exploration of DNA Methylation (DNAm) Dataset and Defining DNAm Subtypes.
(A) DNAm consensus clustering, top 10% variable feature were selected using variance. DNAm subtypes were defined as desribed for mRNA and RPPA subtypes. **(B)** PCA plot and **(C)** DNAm heatmap generated using top variable features show to see DNAm relationship between distinct DNAm subtypes. **(D)** Sankey diagram showing relationship between cell line mRNA and DNAm subtypes. **(E)** DNA methylation instability score in BRCA tumors (TCGA) vs. BRCA cell lines (ICLE and Sanger) and **(F)** DNA methylation instability score across different histological subtypes.

Supplementary Figure S5. Overview of Key ILC and NST Molecular Alterations.
(A) Key Molecular Alterations Enriched in Luminal-A ILC and NST tumors in TCGA dataset. **(B)** Frequency of these alterations in ILC/ILC-like cell lines. **(C)** Allele frequency of these alterations in all NST/IDC, non-basal NST/IDC, ILC and ILC-like cell lines.

Supplementary Figure S6. Differential DNA Methylation Analysis of TCGA Luminal-A ILC vs NST Tumors.
(A) *TFAP2B* expression in ILC, ILC-like and NST cell lines showing most ILC/ILC-like genes have high *TFAP2B* expression. **(B)** Volcano plot showing differentially methylated probes in TCGA Luminal A ILC vs NST tumors annotated by associated gene names (and region). **(C)** Genes with most frequently methylated probes from panel B.

Supplementary Figure S7. p120-catenin, E-cadherin and Hoechst immunofluorescence staining of 17 ILC/ILC-like cell lines.
Immunofluorescence of p120-catenin (1st column), E-cadherin (2nd column), Hoechst nuclear staining (3rd column) and merge of these stainings (4th column) across ILC (names in red), ILC-like (names in purple) and NST (name in blue) cell lines. All ILC/ILC-like cell lines had *CDH1* and *CTNNA1* gene defects resulting in loss of E-cadherin/α-catenin and relocalized of p120-catenin from memberane to cytoplasm. For comparison, we show a *CDH1*/*CTNNA1* WT NST cell line (MCF7) with memberanous staining of both p120 and E-cadherin.

964 **Supplementary Figure S8. Whole-Genome Landscape of ILC/ILC-like Cell Lines.**
965 Circos plots showing OGM identified structural rearrangments, SNP array based copy number, and shatterseek
966 identified chromothripsis events across 17 ILC/ILC-like Cell Lines.
967

968 **Supplementary Figure S9. Association Between Various Genomic Metrics of Genomic Instability.**
969 **(A)** Pearson Correlation between SNV/Mutation count and SV count. **(B)** Barplot showing chromosome size in MBs
970 (megabases). **(C)** SV count across chromosomes. **(D)** Mutation count across chromosomes. **(E)** Pearson correlation
971 between chromosome size and SV count (excluding translocations). **(F)** Pearson correlation bewtween
972 chromosome size and SV counts. **(G)** Pearson correlation between chromosome size and mutation count.
973

974 **Supplementary Figure S10. Overview of Functional Fusions.**
975 **(A)** Functional (gain of expression or loss of expression) fusions identified via integrative analysis of OGM and
976 RNAseq datasets across 17 ILC/ILC-like cell lines. Each fusion pair is annotated by cell line, structural alteration type
977 (AltType), fusion gene A and B annotation as oncogene or tumor suppressor (OncoTS) and affect on gene A or gene
978 B expression **(B)** Recurrently fused genes including *BCAS3, GRB7, PPM1D, SHANK2, SKAPI* and *TENM4*. **(C)**
979 Recurrent fusions of *PPM1D* and *GRB7* genes.
980

981 **Supplementary Figure S11. Ingenuity Pathway Analysis (IPA) of Consensus Differential Dependencies.**
982 **(A)** The top strong/high dependency and weak/low dependency pathways identified IPA analysis of consensus
983 differential dependencies. **(B)** Table showing genes (last column) associated with the pathways shown in A.
984

985 **Supplementary Figure S12. Molecular Alterations in Key Breast Cancer Pathways in ILC/ILC-like cell lines.**
986 Molecular alterations in key breast cancer pathways including (Cell Cycle and TP53 pathway, RTK-RAS pathway,
987 PI3K/AKT pathway and DNA damage repair (DDR) pathway genes).
988

989

Bibliography

1. Mamtani A, King TA. Lobular Breast Cancer: Different Disease, Different Algorithms? Surgical Oncology Clinics of North America. 2018.
2. Christgen M, Cserni G, Floris G, Marchio C, Djerroudi L, Kreipe H, et al. Lobular Breast Cancer: Histomorphology and Different Concepts of a Special Spectrum of Tumors. Cancers (Basel) [Internet]. 2021 Aug 1 [cited 2023 Jul 16];13(15):3695. Available from: /pmc/articles/PMC8345067/
3. Ciriello G, Gatza MLML, Beck AHAH, Wilkerson MD, Rhie SK, Pastore A, et al. Comprehensive Molecular Portraits of Invasive Lobular Breast Cancer. Cell [Internet]. 2015 Oct 8 [cited 2023 Jul 16];163(2):506–19. Available from: https://pubmed.ncbi.nlm.nih.gov/26451490/
4. Desmedt C, Zoppoli G, Gundem G, Pruneri G, Larsimont D, Fornili M, et al. Genomic Characterization of Primary Invasive Lobular Breast Cancer. In: Journal of Clinical Oncology. 2016.
5. Luveta J, Parks RM, Heery DM, Cheung KL, Johnston SJ. Invasive Lobular Breast Cancer as a Distinct Disease: Implications for Therapeutic Strategy. Oncol Ther. 2020 Jun;8(1):1–11.
6. Van Baelen K, Geukens T, Maetens M, Tjan-Heijnen V, Lord CJ, Linn S, et al. Current and future diagnostic and treatment strategies for patients with invasive lobular breast cancer. Ann Oncol [Internet]. 2022 Aug 1 [cited 2023 Jul 16];33(8):769–85. Available from: https://pubmed.ncbi.nlm.nih.gov/35605746/

7. Oesterreich S, Nasrazadani A, Zou J, Carleton N, Onger T, Wright MD, et al. Clinicopathological Features and Outcomes Comparing Patients With Invasive Ductal and Lobular Breast Cancer. J Natl Cancer Inst [Internet]. 2022 Nov 1 [cited 2023 Jul 16];114(11):1511–22. Available from: https://pubmed.ncbi.nlm.nih.gov/36239760/

8. Sflomos G, Schipper K, Koorman T, Fitzpatrick A, Oesterreich S, Lee A V., et al. Atlas of Lobular Breast Cancer Models: Challenges and Strategic Directions. Cancers (Basel) [Internet]. 2021 Nov 1 [cited 2023 Jul 16];13(21). Available from: https://pubmed.ncbi.nlm.nih.gov/34771558/

9. Christgen M, Derksen PWB. Lobular breast cancer: Molecular basis, mouse and cellular models [Internet]. Breast Cancer Research Breast Cancer Res; Feb 8, 2015. Available from: https://pubmed.ncbi.nlm.nih.gov/25757734/

10. Sikora MJ, Cooper KL, Bahreini A, Luthra S, Wang G, Chandran UR, et al. Invasive lobular carcinoma cell lines are characterized by unique estrogen-mediated gene expression patterns and altered tamoxifen response. Cancer Res. 2014;

11. Ghandi M, Huang FW, Jané-Valbuena J, Kryukov G V., Lo CC, McDonald ER, et al. Next-generation characterization of the Cancer Cell Line Encyclopedia. Nature. 2019;

12. Marcotte R, Sayad A, Brown KR, Sanchez-Garcia F, Reimand J, Haider M, et al. Functional Genomic Landscape of Human Breast Cancer Drivers, Vulnerabilities, and Resistance. Cell [Internet]. 2016 Jan 14 [cited 2023 Jul 16];164(1–2):293–309. Available from: https://pubmed.ncbi.nlm.nih.gov/26771497/

13. Iorio F, Knijnenburg TA, Vis DJ, Bignell GR, Menden MP, Schubert M, et al. A Landscape of Pharmacogenomic Interactions in Cancer. Cell [Internet]. 2016 Jul 28 [cited 2023 Jul 16];166(3):740–54. Available from: https://pubmed.ncbi.nlm.nih.gov/27397505/

14. Daemen A, Griffith OL, Heiser LM, Wang NJ, Enache OM, Sanborn Z, et al. Modeling precision treatment of breast cancer. Genome Biol [Internet]. 2013 Dec 10 [cited 2023 Jul 16];14(10). Available from: https://pubmed.ncbi.nlm.nih.gov/24176112/

15. Garnett MJ, Edelman EJ, Heidorn SJ, Greenman CD, Dastur A, Lau KW, et al. Systematic identification of genomic markers of drug sensitivity in cancer cells. Nature. 2012;

16. Tsherniak A, Vazquez F, Montgomery PG, Weir BA, Kryukov G, Cowley GS, et al. Defining a Cancer Dependency Map. Cell [Internet]. 2017 Jul 27 [cited 2023 Jul 16];170(3):564-576.e16. Available from: https://pubmed.ncbi.nlm.nih.gov/28753430/

17. Knijnenburg TA, Klau GW, Iorio F, Garnett MJ, McDermott U, Shmulevich I, et al. Logic models to predict continuous outputs based on binary inputs with an application to personalized cancer therapy. Sci Rep [Internet]. 2016 Nov 23 [cited 2023 Jul 16];6. Available from: https://pubmed.ncbi.nlm.nih.gov/27876821/

18. Soysal E, Lee HJ, Zhang Y, Huang LCC, Chen X, Wei Q, et al. CATTLE (CAncer treatment treasury with linked evidence): An integrated knowledge base for personalized oncology research and practice. CPT Pharmacometrics Syst Pharmacol [Internet]. 2017 Mar 1 [cited 2023 Jul 16];6(3):188–96. Available from: https://pubmed.ncbi.nlm.nih.gov/28296354/

19. Sheng J, Li F, Wong STC. Optimal drug prediction from personal genomics profiles. IEEE J Biomed Health Inform [Internet]. 2015 Jul 1 [cited 2023 Jul 16];19(4):1264–70. Available from: https://pubmed.ncbi.nlm.nih.gov/25781964/

20. Ammad-Ud-Din M, Georgii E, Gönen M, Laitinen T, Kallioniemi O, Wennerberg K, et al. Integrative and personalized QSAR analysis in cancer by kernelized Bayesian matrix factorization. J Chem Inf Model [Internet]. 2014 Aug 25 [cited 2023 Jul 16];54(8):2347–59. Available from: https://pubmed.ncbi.nlm.nih.gov/25046554/

21. Naulaerts S, Dang CC, Ballester PJ. Precision and recall oncology: combining multiple gene mutations for improved identification of drug-sensitive tumours. Oncotarget [Internet]. 2017 [cited 2023 Jul 16];8(57):97025–40. Available from: https://pubmed.ncbi.nlm.nih.gov/29228590/

22. Ching KA, Wang K, Kan Z, Fernandez J, Zhong W, Kostrowicki J, et al. Cell index database (CELLX): A web tool for cancer precision medicine. Pacific Symposium on Biocomputing. 2015;10–9.

23. Marcotte R, Sayad A, Brown KR, Sanchez-Garcia F, Reimand J, Haider M, et al. Functional Genomic Landscape of Human Breast Cancer Drivers, Vulnerabilities, and Resistance. Cell [Internet]. 2016 Jan 14 [cited 2023 Jul 16];164(1–2):293–309. Available from: https://pubmed.ncbi.nlm.nih.gov/26771497/

24. Sikora MJ, Jankowitz RC, Dabbs DJ, Oesterreich S. Invasive lobular carcinoma of the breast: Patient response to systemic endocrine therapy and hormone response in model systems. In: Steroids. 2013.

25. Tasdemir N, Bossart EA, Li Z, Zhu L, Sikora MJ, Levine KM, et al. Comprehensive phenotypic characterization human invasive lobular carcinoma cell lines in 2D and 3D cultures. Cancer Res. 2018;

26. Du T, Sikora MJ, Levine KM, Tasdemir N, Riggins RB, Wendell SG, et al. Key regulators of lipid metabolism drive endocrine resistance in invasive lobular breast cancer. Breast Cancer Research. 2018;

27. Levine KM, Priedigkeit N, Basudan A, Tasdemir N, Sikora MJ, Sokol ES, et al. FGFR4 overexpression and hotspot mutations in metastatic ER+ breast cancer are enriched in the lobular subtype. NPJ Breast Cancer. 2019;

28. Christgen M, Kandt LD, Antonopoulos W, al. et. Inter-observer agreement for the histological diagnosis of invasive lobular breast carcinoma. J Pathol Clin Res. 2022;8:191–205.

29. Michaut M, Chin SF, Majewski I, Severson TM, Bismeijer T, De Koning L, et al. Integration of genomic, transcriptomic and proteomic data identifies two biologically distinct subtypes of invasive lobular breast cancer. Sci Rep [Internet]. 2016 Jan 5 [cited 2023 Jul 16];6. Available from: https://pubmed.ncbi.nlm.nih.gov/26729235/

30. Elangovan A, Bossart EA, Basudan A, Tasdemir N, Shah OS, Ding K, et al. WCRC-25: A novel luminal Invasive Lobular Carcinoma cell line model. bioRxiv [Internet]. 2023 Sep 17 [cited 2023 Sep 25];2023.09.15.558023. Available from: https://www.biorxiv.org/content/10.1101/2023.09.15.558023v1

31. Tibes R, Qiu YH, Lu Y, Hennessy B, Andreeff M, Mills GB, et al. Reverse phase protein array: validation of a novel proteomic technology and utility for analysis of primary leukemia specimens and hematopoietic stem cells. Mol Cancer Ther [Internet]. 2006 Oct [cited 2023 Jul 17];5(10):2512–21. Available from: https://pubmed.ncbi.nlm.nih.gov/17041095/

32. S. A. FastQC [Internet]. 2010. Available from: http://www.bioinformatics.babraham.ac.uk/projects/fastqc

33. Ewels P, Magnusson M, Lundin S, Käller M. MultiQC: summarize analysis results for multiple tools and samples in a single report. Bioinformatics [Internet]. 2016 Oct 1 [cited 2023 Jul 17];32(19):3047–8. Available from: https://dx.doi.org/10.1093/bioinformatics/btw354

34. Dobin A, Davis CA, Schlesinger F, Drenkow J, Zaleski C, Jha S, et al. STAR: Ultrafast universal RNA-seq aligner. Bioinformatics [Internet]. 2013 Jan 1 [cited 2019 Apr 21];29(1):15–21. Available from: http://www.ncbi.nlm.nih.gov/pubmed/23104886

35. Liao Y, Smyth GK, Shi W. featureCounts: an efficient general purpose program for assigning sequence reads to genomic features. Bioinformatics [Internet]. 2014 Apr 1 [cited 2023 Jul 17];30(7):923–30. Available from: https://pubmed.ncbi.nlm.nih.gov/24227677/

36. Robinson MD, McCarthy DJ, Smyth GK. edgeR: a Bioconductor package for differential expression analysis of digital gene expression data. Bioinformatics [Internet]. 2010 Nov 11 [cited 2023 Jul 17];26(1):139–40. Available from: https://pubmed.ncbi.nlm.nih.gov/19910308/

37. R Development Core Team. R: A Language and Environment for Statistical Computing. R Foundation for Statistical Computing. 2016;

38. Symmans WF, Hatzis C, Sotiriou C, Andre F, Peintinger F, Regitnig P, et al. Genomic index of sensitivity to endocrine therapy for breast cancer. J Clin Oncol [Internet]. 2010 Sep 20 [cited 2023 Jul 17];28(27):4111–9. Available from: https://pubmed.ncbi.nlm.nih.gov/20697068/

39. Li H, Durbin R. Fast and accurate short read alignment with Burrows-Wheeler transform. Bioinformatics. 2009;

40. Cibulskis K, Lawrence MS, Carter SL, Sivachenko A, Jaffe D, Sougnez C, et al. Sensitive detection of somatic point mutations in impure and heterogeneous cancer samples. Nat Biotechnol [Internet]. 2013 Mar [cited 2023 Jul 17];31(3):213–9. Available from: https://pubmed.ncbi.nlm.nih.gov/23396013/

41. McLaren W, Gil L, Hunt SE, Riat HS, Ritchie GRS, Thormann A, et al. The Ensembl Variant Effect Predictor. Genome Biol [Internet]. 2016 Jun 6 [cited 2023 Jul 17];17(1). Available from: https://pubmed.ncbi.nlm.nih.gov/27268795/

42. Altshuler DM, Durbin RM, Abecasis GR, Bentley DR, Chakravarti A, Clark AG, et al. An integrated map of genetic variation from 1,092 human genomes. Nature 2012 491:7422 [Internet]. 2012 Oct 31 [cited 2023 Jul 17];491(7422):56–65. Available from: https://www.nature.com/articles/nature11632

43. Mayakonda A, Lin DC, Assenov Y, Plass C, Koeffler HP. Maftools: Efficient and comprehensive analysis of somatic variants in cancer. Genome Res [Internet]. 2018 Nov 1 [cited 2023 Jul 17];28(11):1747–56. Available from: /pmc/articles/PMC6211645/

44. Cortés-Ciriano I, Lee JJK, Xi R, Jain D, Jung YL, Yang L, et al. Comprehensive analysis of chromothripsis in 2,658 human cancers using whole-genome sequencing. Nat Genet [Internet]. 2020 Mar 1 [cited 2023 Jul 17];52(3):331–41. Available from: https://pubmed.ncbi.nlm.nih.gov/32025003/

45. Cui Z, Cui Y, Zang T, Wang Y. interacCircos: an R package based on JavaScript libraries for the generation of interactive circos plots. Bioinformatics [Internet]. 2021 Oct 15 [cited 2023 Jul 17];37(20):3642–4. Available from: https://pubmed.ncbi.nlm.nih.gov/33830205/

46. Zhou W, Triche TJ, Laird PW, Shen H. SeSAMe: reducing artifactual detection of DNA methylation by Infinium BeadChips in genomic deletions. Nucleic Acids Res [Internet]. 2018 [cited 2023 Jul 17];46(20). Available from: https://pubmed.ncbi.nlm.nih.gov/30085201/

47. Zhou W, Laird PW, Shen H. Comprehensive characterization, annotation and innovative use of Infinium DNA methylation BeadChip probes. Nucleic Acids Res [Internet]. 2017

Feb 28 [cited 2023 Jul 17];45(4):e22–e22. Available from: https://dx.doi.org/10.1093/nar/gkw967

48. Seshan VE O. DNAcopy. Bioconductor; 2023.

49. Mermel CH, Schumacher SE, Hill B, Meyerson ML, Beroukhim R, Getz G. GISTIC2.0 facilitates sensitive and confident localization of the targets of focal somatic copy-number alteration in human cancers. Genome Biol [Internet]. 2011 Apr 28 [cited 2023 Jul 17];12(4):1–14. Available from: https://genomebiology.biomedcentral.com/articles/10.1186/gb-2011-12-4-r41

50. Oza VH, Fisher JL, Darji R, Lasseigne BN. CINmetrics: an R package for analyzing copy number aberrations as a measure of chromosomal instability. PeerJ [Internet]. 2023 [cited 2023 Jul 17];11. Available from: https://pubmed.ncbi.nlm.nih.gov/37123011/

51. Gendoo DMA, Ratanasirigulchai N, Schröder MS, Paré L, Parker JS, Prat A, et al. Genefu: an R/Bioconductor package for computation of gene expression-based signatures in breast cancer. Bioinformatics [Internet]. 2016 Apr 1 [cited 2023 Jul 17];32(7):1097–9. Available from: https://dx.doi.org/10.1093/bioinformatics/btv693

52. Bernard PS, Parker JS, Mullins M, Cheung MCU, Leung S, Voduc D, et al. Supervised Risk Predictor of Breast Cancer Based on Intrinsic Subtypes. Journal of Clinical Oncology [Internet]. 2009 Mar 3 [cited 2023 Jul 16];27(8):1160. Available from: /pmc/articles/PMC2667820/

53. Wilkerson MD, Hayes DN. ConsensusClusterPlus: A class discovery tool with confidence assessments and item tracking. Bioinformatics. 2010 Apr;26(12):1572–3.

54. Li Q, Jiang B, Guo J, Shao H, Del Priore IS, Chang Q, et al. INK4 Tumor Suppressor Proteins Mediate Resistance to CDK4/6 Kinase Inhibitors. Cancer Discov [Internet]. 2022

[cited 2023 Jul 17];12(2):356–71. Available from: https://pubmed.ncbi.nlm.nih.gov/34544752/

55. Gao J, Aksoy BA, Dogrusoz U, Dresdner G, Gross B, Sumer SO, et al. Integrative analysis of complex cancer genomics and clinical profiles using the cBioPortal. Sci Signal [Internet]. 2013 Apr 2 [cited 2023 Jul 17];6(269). Available from: https://pubmed.ncbi.nlm.nih.gov/23550210/

56. Thorvaldsdóttir H, Robinson JT, Mesirov JP. Integrative Genomics Viewer (IGV): high-performance genomics data visualization and exploration. Brief Bioinform [Internet]. 2013 Mar [cited 2023 Jul 17];14(2):178–92. Available from: https://pubmed.ncbi.nlm.nih.gov/22517427/

57. Mateo J, Chakravarty D, Dienstmann R, Jezdic S, Gonzalez-Perez A, Lopez-Bigas N, et al. A framework to rank genomic alterations as targets for cancer precision medicine: the ESMO Scale for Clinical Actionability of molecular Targets (ESCAT). Ann Oncol [Internet]. 2018 Sep 1 [cited 2023 Jul 17];29(9):1895–902. Available from: https://pubmed.ncbi.nlm.nih.gov/30137196/

58. Sanchez-Vega F, Mina M, Armenia J, Chatila WK, Luna A, La KC, et al. Oncogenic Signaling Pathways in The Cancer Genome Atlas. Cell [Internet]. 2018 Apr 5 [cited 2023 Jul 17];173(2):321-337.e10. Available from: https://pubmed.ncbi.nlm.nih.gov/29625050/

59. Zhou X, Edmonson MN, Wilkinson MR, Patel A, Wu G, Liu Y, et al. Exploring genomic alteration in pediatric cancer using ProteinPaint. Nat Genet [Internet]. 2016 Dec 29 [cited 2023 Jul 17];48(1):4–6. Available from: https://pubmed.ncbi.nlm.nih.gov/26711108/

60. Elangovan A, Hooda J, Savariau L, Puthanmadhomnarayanan S, Yates ME, Chen J, et al. Loss of E-cadherin Induces IGF1R Activation and Reveals a Targetable Pathway in

Invasive Lobular Breast Carcinoma. Mol Cancer Res [Internet]. 2022 Sep 1 [cited 2023 Jul 17];20(9):1405–19. Available from: https://pubmed.ncbi.nlm.nih.gov/35665642/

61. Silva TC, Coetzee SG, Gull N, Yao L, Hazelett DJ, Noushmehr H, et al. ELMER v.2: an R/Bioconductor package to reconstruct gene regulatory networks from DNA methylation and transcriptome profiles. Bioinformatics [Internet]. 2019 Jun 1;35(11):1974–7. Available from: https://doi.org/10.1093/bioinformatics/bty902

62. Ritchie ME, Phipson B, Wu D, Hu Y, Law CW, Shi W, et al. limma powers differential expression analyses for RNA-sequencing and microarray studies. Nucleic Acids Res. 2015 Apr;43(7):e47–e47.

63. Yoshihara K, Wang Q, Torres-Garcia W, Zheng S, Vegesna R, Kim H, et al. The landscape and therapeutic relevance of cancer-associated transcript fusions. Oncogene [Internet]. 2015 Sep 10 [cited 2023 Jul 17];34(37):4845–54. Available from: https://pubmed.ncbi.nlm.nih.gov/25500544/

64. Federico A, Monti S. HypeR: An R package for geneset enrichment workflows. Bioinformatics. 2020 Feb;36(4):1307–8.

65. Wagner AH, Coffman AC, Ainscough BJ, Spies NC, Skidmore ZL, Campbell KM, et al. DGIdb 2.0: mining clinically relevant drug-gene interactions. Nucleic Acids Res [Internet]. 2016;44. Available from: https://doi.org/10.1093/nar/gkv1165

66. Gu Z, Eils R, Schlesner M. Complex heatmaps reveal patterns and correlations in multidimensional genomic data. Bioinformatics. 2016;

67. Wickham H. ggplot2: Elegant Graphics for Data Analysis [Internet]. Springer-Verlag New York; 2016. Available from: https://ggplot2.tidyverse.org

68. Christgen M, Bruchhardt H, Hadamitzky C, Rudolph C, Steinemann D, Gadzicki D, et al. Comprehensive genetic and functional characterization of IPH-926: A novel CDHl-null tumour cell line from human lobular breast cancer. Journal of Pathology. 2009;

69. Perou CM, Sørile T, Eisen MB, Van De Rijn M, Jeffrey SS, Ress CA, et al. Molecular portraits of human breast tumours. 2000 Aug 17 [cited 2023 Jul 16];406(6797):747–52. Available from: https://pubmed.ncbi.nlm.nih.gov/10963602/

70. Koboldt DC, Fulton RS, McLellan MD, Schmidt H, Kalicki-Veizer J, McMichael JF, et al. Comprehensive molecular portraits of human breast tumours. Nature [Internet]. 2012 Sep 23 [cited 2023 Jul 16];490(7418):61–70. Available from: https://doi.org/10.1038/nature11412

71. Neve RM, Chin K, Fridlyand J, Yeh J, Baehner FL, Fevr T, et al. A collection of breast cancer cell lines for the study of functionally distinct cancer subtypes. Cancer Cell [Internet]. 2006 [cited 2023 Jul 17];10(6):515. Available from: /pmc/articles/PMC2730521/

72. Weigman VJ, Chao HH, Shabalin AA, He X, Parker JS, Nordgard SH, et al. Basal-like Breast cancer DNA copy number losses identify genes involved in genomic instability, response to therapy, and patient survival. Breast Cancer Res Treat [Internet]. 2012 Jun [cited 2023 Jul 17];133(3):865. Available from: /pmc/articles/PMC3387500/

73. Derksen PWB, Liu X, Saridin F, van der Gulden H, Zevenhoven J, Evers B, et al. Somatic inactivation of E-cadherin and p53 in mice leads to metastatic lobular mammary carcinoma through induction of anoikis resistance and angiogenesis. Cancer Cell [Internet]. 2006 [cited 2023 Jul 17];10(5):437–49. Available from: https://pubmed.ncbi.nlm.nih.gov/17097565/

74. Graziano F, Humar B, Guilford P. The role of the E-cadherin gene (CDH1) in diffuse gastric cancer susceptibility: from the laboratory to clinical practice. Ann Oncol [Internet]. 2003

Dec [cited 2023 Jul 17];14(12):1705–13. Available from: https://pubmed.ncbi.nlm.nih.gov/14630673/

75. Bolkestein M, Wong JKL, Thewes V, Körber V, Hlevnjak M, Elgaafary S, et al. Chromothripsis in Human Breast Cancer. Cancer Res [Internet]. 2020 Nov 15 [cited 2023 Jul 17];80(22):4918–31. Available from: https://pubmed.ncbi.nlm.nih.gov/32973084/

76. Cai H, Kumar N, Bagheri HC, von Mering C, Robinson MD, Baudis M. Chromothripsis-like patterns are recurring but heterogeneously distributed features in a survey of 22,347 cancer genome screens. BMC Genomics [Internet]. 2014 Jan 29 [cited 2023 Jul 17];15(1). Available from: https://pubmed.ncbi.nlm.nih.gov/24476156/

77. Ennour-Idrissi K, Dragic D, Issa E, Michaud A, Chang SL, Provencher L, et al. DNA Methylation and Breast Cancer Risk: An Epigenome-Wide Study of Normal Breast Tissue and Blood. Cancers (Basel) [Internet]. 2020 Nov 1 [cited 2023 Sep 23];12(11):1–16. Available from: /pmc/articles/PMC7690691/

78. Ennour-Idrissi K, Dragic D, Durocher F, Diorio C. Epigenome-wide DNA methylation and risk of breast cancer: a systematic review. BMC Cancer [Internet]. 2020 Dec 1 [cited 2023 Sep 23];20(1). Available from: /pmc/articles/PMC7603741/

79. Joo JE, Dowty JG, Milne RL, Wong EM, Dugué PA, English D, et al. Heritable DNA methylation marks associated with susceptibility to breast cancer. Nature Communications 2018 9:1 [Internet]. 2018 Feb 28 [cited 2023 Sep 23];9(1):1–12. Available from: https://www.nature.com/articles/s41467-018-03058-6

80. Batra RN, Lifshitz A, Vidakovic AT, Chin SF, Sati-Batra A, Sammut SJ, et al. DNA methylation landscapes of 1538 breast cancers reveal a replication-linked clock, epigenomic instability and cis-regulation. Nature Communications 2021 12:1 [Internet]. 2021 Sep 13

[cited 2023 Sep 23];12(1):1–13. Available from: https://www.nature.com/articles/s41467-021-25661-w

81. Fleischer T, Tekpli X, Mathelier A, Wang S, Nebdal D, Dhakal HP, et al. DNA methylation at enhancers identifies distinct breast cancer lineages. Nature Communications 2017 8:1 [Internet]. 2017 Nov 9 [cited 2023 Sep 23];8(1):1–14. Available from: https://www.nature.com/articles/s41467-017-00510-x

82. Wei B, Wu F, Xing W, Sun H, Yan C, Zhao C, et al. A panel of DNA methylation biomarkers for detection and improving diagnostic efficiency of lung cancer. Scientific Reports 2021 11:1 [Internet]. 2021 Aug 18 [cited 2023 Sep 23];11(1):1–10. Available from: https://www.nature.com/articles/s41598-021-96242-6

83. Ibrahim J, Peeters M, Van Camp G, Op de Beeck K. Methylation biomarkers for early cancer detection and diagnosis: Current and future perspectives. Eur J Cancer. 2023 Jan 1;178:91–113.

84. Cox MC, Deng C, Naler LB, Lu C, Verbridge SS. Effects of culture condition on epigenomic profiles of brain tumor cells. ACS Biomater Sci Eng [Internet]. 2019 Mar 3 [cited 2023 Sep 23];5(3):1544. Available from: /pmc/articles/PMC6886720/

85. Rodger EJ, Almomani SN, Ludgate JL, Stockwell PA, Baguley BC, Eccles MR, et al. Comparison of global dna methylation patterns in human melanoma tissues and their derivative cell lines. Cancers (Basel) [Internet]. 2021 May 1 [cited 2023 Sep 23];13(9). Available from: /pmc/articles/PMC8124222/

86. Christgen M, Cserni G, Floris G, Marchio C, Djerroudi L, Kreipe H, et al. Lobular Breast Cancer: Histomorphology and Different Concepts of a Special Spectrum of Tumors.

Cancers (Basel) [Internet]. 2021 Aug 1 [cited 2023 Jul 17];13(15). Available from: https://pubmed.ncbi.nlm.nih.gov/34359596/

87. Raap M, Gierendt L, Kreipe HH, Christgen M. Transcription factor AP-2beta in development, differentiation and tumorigenesis. Int J Cancer [Internet]. 2021 Sep 15 [cited 2023 Jul 17];149(6):1221–7. Available from: https://pubmed.ncbi.nlm.nih.gov/33720400/

88. Raap M, Gronewold M, Christgen H, Glage S, Bentires-Alj M, Koren S, et al. Lobular carcinoma in situ and invasive lobular breast cancer are characterized by enhanced expression of transcription factor AP-2β. Lab Invest [Internet]. 2018 Jan 1 [cited 2023 Jul 17];98(1):117–29. Available from: https://pubmed.ncbi.nlm.nih.gov/29035379/

89. Yoldi G, Pellegrini P, Trinidad EM, Cordero A, Gomez-Miragaya J, Serra-Musach J, et al. RANK Signaling Blockade Reduces Breast Cancer Recurrence by Inducing Tumor Cell Differentiation. Cancer Res [Internet]. 2016 Oct 1 [cited 2023 Jul 17];76(19):5857–69. Available from: https://pubmed.ncbi.nlm.nih.gov/27480274/

90. Godwin TD, Kelly ST, Brew TP, Bougen-Zhukov NM, Single AB, Chen A, et al. E-cadherin-deficient cells have synthetic lethal vulnerabilities in plasma membrane organisation, dynamics and function. Gastric Cancer [Internet]. 2019 Mar 15 [cited 2023 Jul 17];22(2):273–86. Available from: https://pubmed.ncbi.nlm.nih.gov/30066183/

91. Telford BJ, Chen A, Beetham H, Frick J, Brew TP, Gould CM, et al. Synthetic Lethal Screens Identify Vulnerabilities in GPCR Signaling and Cytoskeletal Organization in E-Cadherin-Deficient Cells. Mol Cancer Ther [Internet]. 2015 May 1 [cited 2023 Jul 17];14(5):1213–23. Available from: https://pubmed.ncbi.nlm.nih.gov/25777964/

92. Elangovan A, Hooda J, Savariau L, Puthanmadhomnarayanan S, Yates ME, Chen J, et al. Loss of E-cadherin Induces IGF1R Activation and Reveals a Targetable Pathway in

Invasive Lobular Breast Carcinoma. Mol Cancer Res [Internet]. 2022 Sep 1 [cited 2023 Jul 17];20(9):1405–19. Available from: https://pubmed.ncbi.nlm.nih.gov/35665642/

93. Bajrami I, Marlow R, van De Ven M, Brough R, Pemberton HN, Frankum J, et al. E-Cadherin/ROS1 Inhibitor Synthetic Lethality in Breast Cancer. Cancer Discov [Internet]. 2018 Apr 1 [cited 2023 Jul 17];8(4):498–515. Available from: https://pubmed.ncbi.nlm.nih.gov/29610289/

94. Agostinetto E, Nader-Marta G, Paesmans M, Ameye L, Veys I, Buisseret L, et al. ROSALINE: a phase II, neoadjuvant study targeting ROS1 in combination with endocrine therapy in invasive lobular carcinoma of the breast. Future Oncol [Internet]. 2022 Jul 1 [cited 2023 Jul 16];18(22):2383–92. Available from: https://pubmed.ncbi.nlm.nih.gov/35695563/

95. Travis RC, Key TJ. Oestrogen exposure and breast cancer risk. Breast Cancer Res [Internet]. 2003 [cited 2023 Jul 17];5(5):239. Available from: /pmc/articles/PMC314432/

96. André F, Ciruelos E, Rubovszky G, Campone M, Loibl S, Rugo HS, et al. Alpelisib for PIK3CA-Mutated, Hormone Receptor-Positive Advanced Breast Cancer. N Engl J Med [Internet]. 2019 May 16 [cited 2023 Jul 16];380(20):1929–40. Available from: https://pubmed.ncbi.nlm.nih.gov/31091374/

97. Dean L. Trastuzumab (Herceptin) Therapy and ERBB2 (HER2) Genotype. Medical Genetics Summaries. 2012.

98. Voutsadakis IA, Stravodimou A. Homologous Recombination Defects and Mutations in DNA Damage Response (DDR) Genes Besides BRCA1 and BRCA2 as Breast Cancer Biomarkers for PARP Inhibitors and Other DDR Targeting Therapies. Anticancer Res. 2023 Mar 1;43(3):967–81.

99. Djerroudi L, Cabel L, Bidard FC, Vincent-Salomon A. Invasive Lobular Carcinoma of the Breast: Toward Tailoring Therapy? JNCI: Journal of the National Cancer Institute [Internet]. 2022 Nov 14 [cited 2023 Jul 16];114(11):1434–6. Available from: https://dx.doi.org/10.1093/jnci/djac159

100. Reed MEMC, Kutasovic JR, Lakhani SR, Simpson PT. Invasive lobular carcinoma of the breast: morphology, biomarkers and ’omics. 2015 Jan;17(1):12.

101. Arpino G, Bardou VJ, Clark GM, Elledge RM, G A, VJ B, et al. Infiltrating lobular carcinoma of the breast: tumor characteristics and clinical outcome. 2004 Feb;6(3).

102. Shale C, Cameron DL, Baber J, Wong M, Cowley MJ, Papenfuss AT, et al. Unscrambling cancer genomes via integrated analysis of structural variation and copy number. Cell Genomics [Internet]. 2022 Apr 4 [cited 2023 Jul 17];2(4):100112. Available from: /pmc/articles/PMC9903802/

103. Zhang CZ, Leibowitz ML, Pellman D. Chromothripsis and beyond: rapid genome evolution from complex chromosomal rearrangements. Genes Dev [Internet]. 2013 Dec 1 [cited 2023 Jul 17];27(23):2513–30. Available from: https://pubmed.ncbi.nlm.nih.gov/24298051/

104. Voronina N, Wong JKL, Hübschmann D, Hlevnjak M, Uhrig S, Heilig CE, et al. The landscape of chromothripsis across adult cancer types. Nat Commun [Internet]. 2020 Dec 1 [cited 2023 Jul 17];11(1):17. Available from: /pmc/articles/PMC7210959/

105. Fu X, Zhang H, Chen Z, Yang Z, Shi D, Liu T, et al. TFAP2B overexpression contributes to tumor growth and progression of thyroid cancer through the COX-2 signaling pathway. Cell Death Dis [Internet]. 2019 Jun 1 [cited 2023 Jul 17];10(6). Available from: /pmc/articles/PMC6529436/

106. Jin C, Luo Y, Liang Z, Li X, Kołat D, Zhao L, et al. Crucial role of the transcription factors family activator protein 2 in cancer: current clue and views. Journal of Translational Medicine 2023 21:1 [Internet]. 2023 Jun 8 [cited 2023 Jul 17];21(1):1–21. Available from: https://translational-medicine.biomedcentral.com/articles/10.1186/s12967-023-04189-1

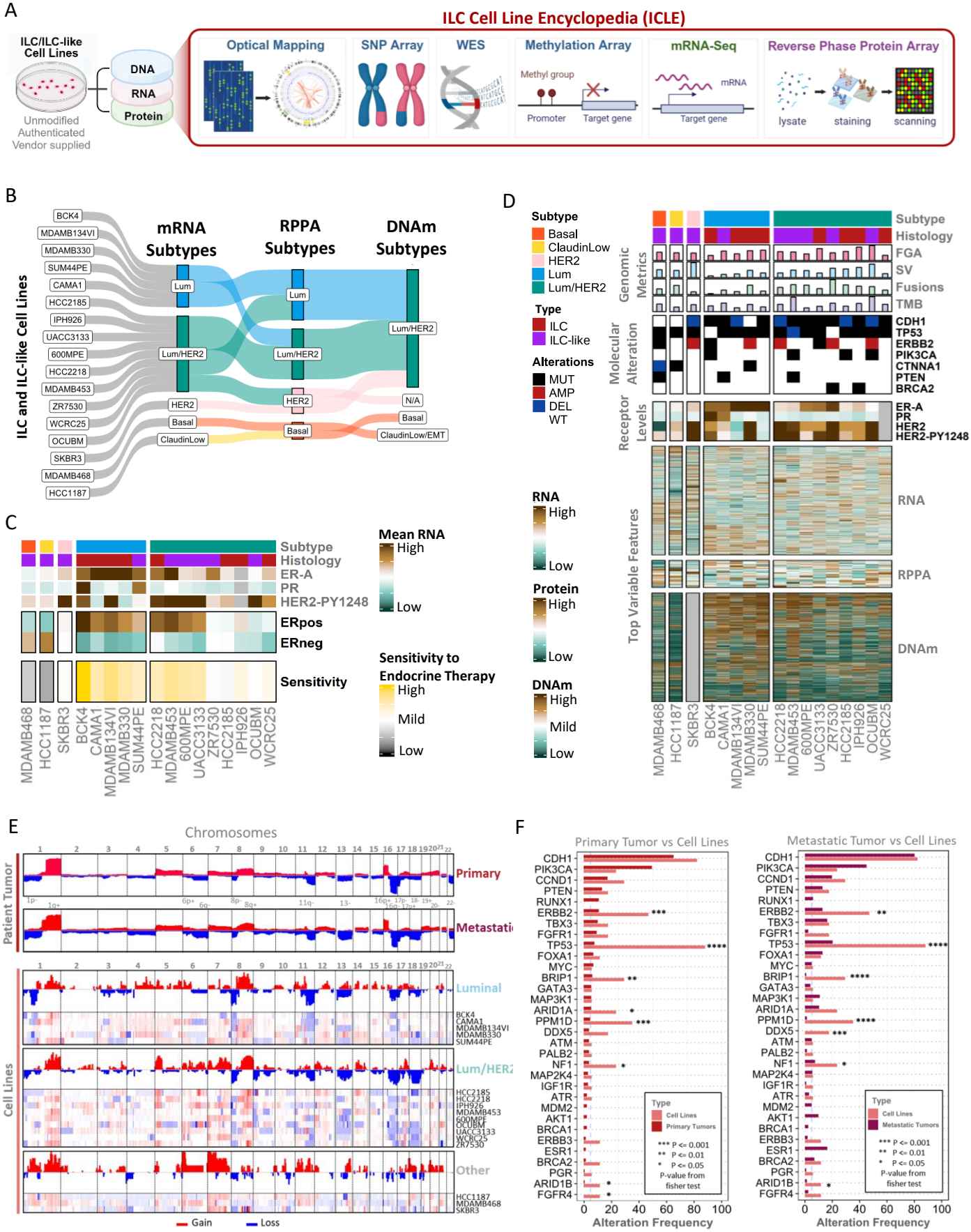

Figure 1. Multi-omic Characterization of ILC and ILC-like Cell Lines and Molecular Resemblance to Human-ILC Disease.

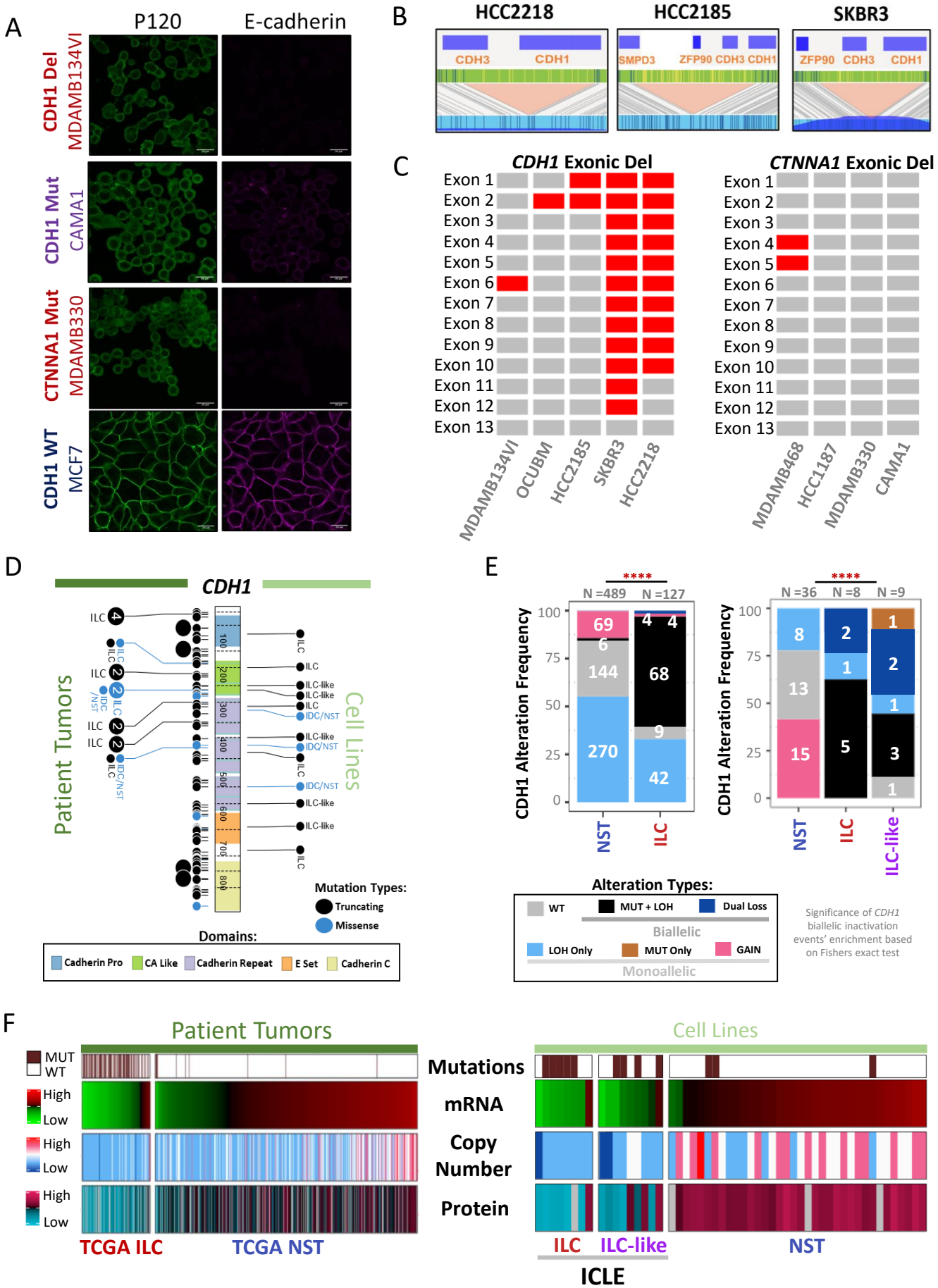

Figure 2. ILC and ILC-like Cell Lines Recapitulate the *CDH1* Alteration Landscape of Human-ILC Disease.

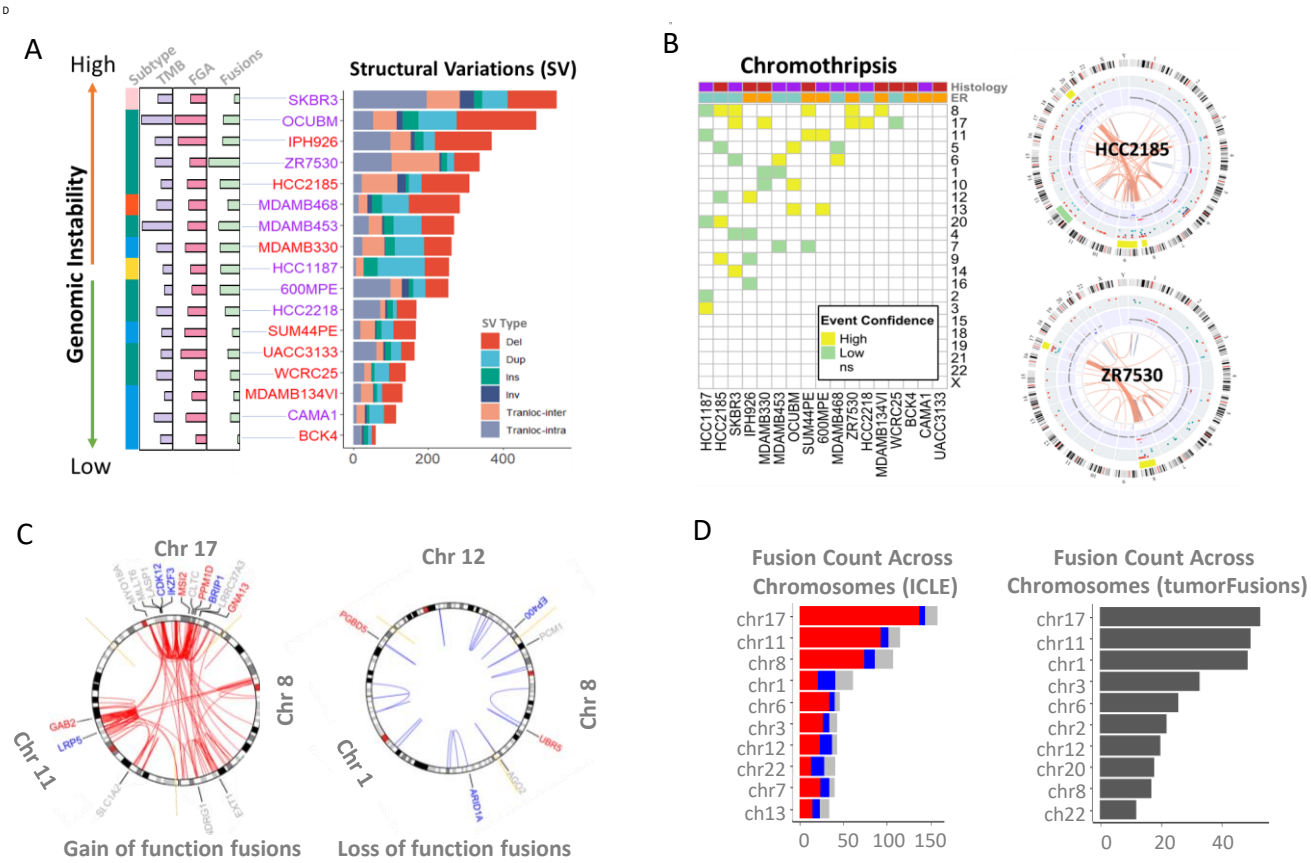

Figure 3. Optical Genome Mapping Unveils Structural Variations, Chromothripsis Events and Functional Gene Fusions.

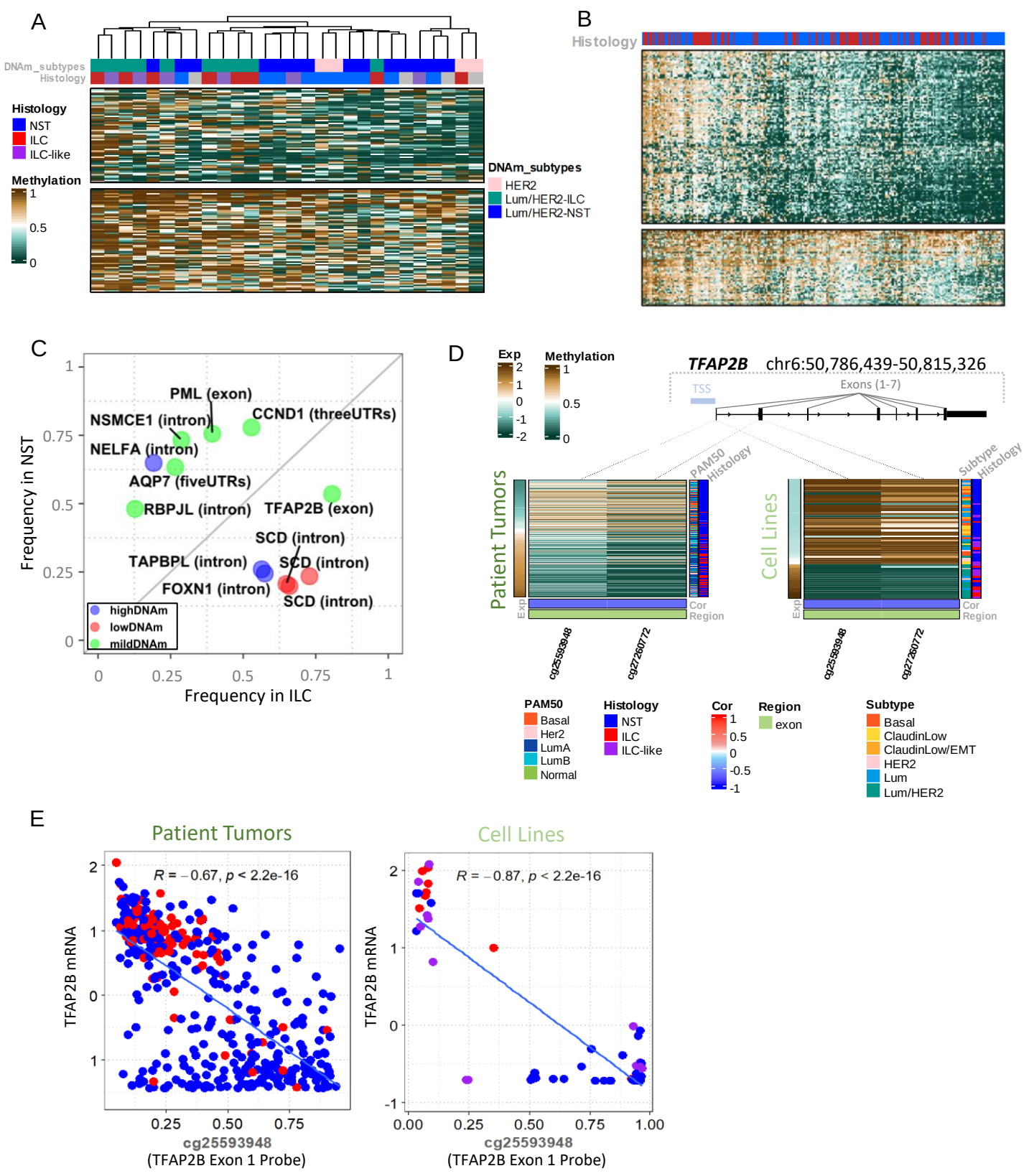

Figure 4. Aberrant DNA Methylation Events and Epigenetic Activation of TFAP2B

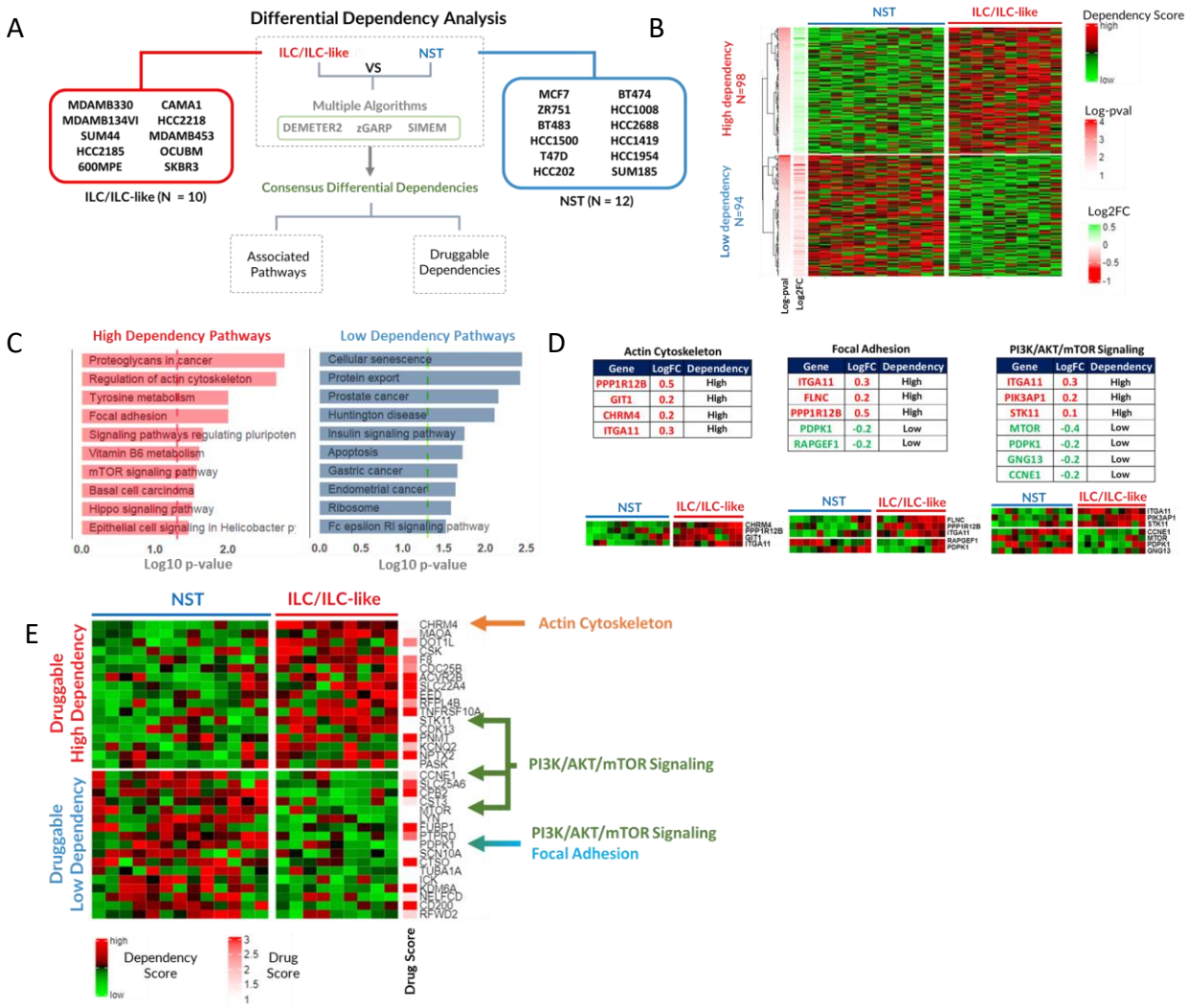

Gene	LogFC	Dependency
PPP1R12B	0.5	High
GIT1	0.2	High
CHRM4	0.2	High
ITGA11	0.3	High

Gene	LogFC	Dependency
ITGA11	0.3	High
FLNC	0.2	High
PPP1R12B	0.5	High
PDPK1	-0.2	Low
RAPGEF1	-0.2	Low

Gene	LogFC	Dependency
ITGA11	0.3	High
PIK3AP1	0.2	High
STK11	0.1	High
MTOR	-0.4	Low
PDPK1	-0.2	Low
GNG13	-0.2	Low
CCNE1	-0.2	Low

Figure 5. Identification of Differential Gene Dependencies in ILC/ILC-like vs NST Cell Lines.

A

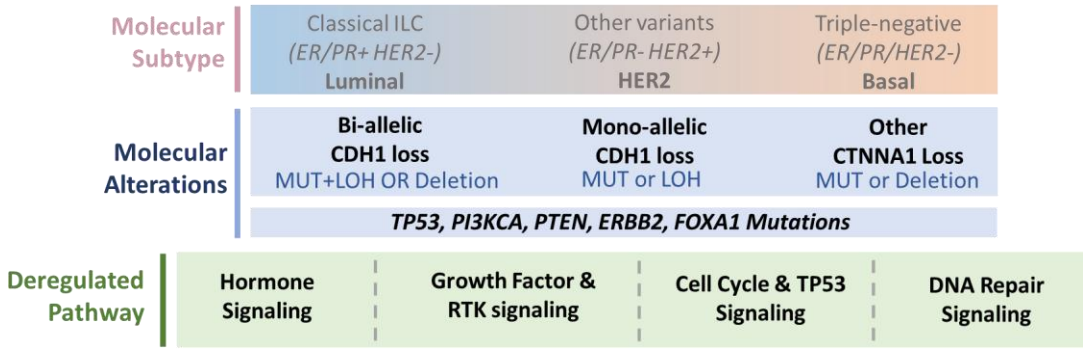

B

		ILC Driver Alterations		Other Altered Genes					Molecular Similarity to ILC Patient Tumors		
Cell Line	Molecular Subtype	CDH1	CTNNA1	TP53	PIK3CA	ERBB2	PTEN	FOXA1	Copy Number	RNA Expression	Suitable Model for ER+/Luminal ILC Disease
BCK4	Lum	MUT;LOH			MUT	MUT			0.5	0.6	Yes
CAMA1	Lum	MUT		MUT;LOH			MUT;LOH		0.3	-0.1	Yes, but low RNA similarity
MDAMB134VI	Lum	EXON6;LOH		MUT;LOH					0.5	0.3	Yes
MDAMB330	Lum		MUT	MUT;LOH		AMP			0.2	0.2	Yes
SUM44PE	Lum	MUT;LOH		MUT;LOH				AMP	0.4	0.2	Yes
600MPE	Lum/HER2	MUT;LOH		MUT;LOH					0.6	0.3	Yes
HCC2185	Lum/HER2	DEL		MUT	MUT;AMP				0.2	NS	Yes, but low RNA similarity
HCC2218	Lum/HER2	DEL		MUT;LOH		AMP			0.5	0.3	Yes
IPH926	Lum/HER2	MUT;LOH		MUT;LOH					0.2	0.3	Yes
MDAMB453	Lum/HER2	MUT;LOH		DEL	MUT;GAIN		MUT	AMP	0.3	0.1	Yes
OCUBM	Lum/HER2	EXON2;LOH		MUT;LOH	MUT;GAIN	AMP			0.3	-0.2	Yes, but low RNA similarity
UACC3133	Lum/HER2	MUT;LOH		MUT;LOH		MUT;GAIN			0.5	0.3	Yes
WCRC25	Lum/HER2	MUT;LOH		MUT;LOH					0.5	0.3	Yes
ZR7530	Lum/HER2	MUT;LOH				AMP			0.5	0.1	Yes
SKBR3	HER2	DEL		MUT;LOH		AMP			0.1	NS	No, HER2 subtype
HCC1187	ClaudinLow		MUT	MUT					0.3	-0.3	No, claudinLow subtype
MDAMB468	Basal		EXON4,5;MUT	MUT;LOH		MUT;LOH	MUT;GAIN		NS	-0.4	No, basal subtype

Alteration
- AMP
- DEL
- MUT
- MUT;AMP
- MUT;DEL
- MUT;GAIN
- MUT;LOH

Figure 6. Scheme for Rational Selection of ILC/ILC-like Cell Lines for Modelling Human-ILC Disease.